T. Hagae

Development of a Large Silica Aerogel Cerenkov Counter and a Study of Momentum Resolution for the Superconducting Kaon Spectrometer

(Master Thesis)

Tomoyuki Hasegawa

Graduate School, University of Tokyo

January 21st, 1991

Abstract

The superconducting kaon spectrometer(SKS) is a superconducting spectrometer system for nuclear physics experiments at intermediate energy. It is to be installed in the north counter hall of National Laboratory for High Energy Physics. The SKS is intended to be useful for hypernuclear spectroscopy by the (π, K) reaction with a good momentum resolution and a large acceptance.

In this thesis, two subjects about the SKS are mainly studied.

One is about silica aerogel Cerenkov counters described in chapter 2. The silica aerogel Cerenkov counters play a very important role in the detector system to veto pions in order to trigger kaon events. Based on conclusions of an experiment for testing a prototype counter and considerations with a Monte Carlo simulation, we design a counter whose size is about 1.2m $\times$ 1.4m and with thickness about 40cm. It is shown that the pion $(0.7GeV/c)$ rejection efficiency is expected to be better than 96.5%. Accordingly the efficiency better than 99.9% can be expected with the two layers.

The other is the momentum resolution of the SKS discussed in chapter 3. The good momentum resolution is one of the most important performance of the SKS. All the factors which influence the resolution are evaluated with a Monte Carlo simulation. It is shown that accurate measurement of the magnetic field is the most crucial in order to achieve the good resolution. In the latter half, energy resolution for the Λ-hypernuclear mass is estimated taking into account the momentum resolution of the SKS and the beam line spectrometer, and the energy loss fluctuation in the target. It is shown that the resolution better than $2MeV$ could be obtained.

Contents

Chapter 1

What is the SKS?

1.1 Introduction

Design of the SKS is optimized for the Λ-hypernuclear spectroscopy by the (π, K) reaction. For this objective, the spectrometer is expected to have good momentum resolution of 0.1%(FWHM) and the large acceptance of 100msr in the momentum region around $1GeV/c$. A beam line spectrometer is also expected to have good momentum resolution better than 0.1%(FWHM) for the momentum around $1GeV/c$. Consequently, energy resolution for the hypernuclear mass is expected to be better than $2MeV$(FWHM). This performance would make it possible to carry out many interesting experiments in the momentum region around $1GeV/c$ as well as the hypernuclear spectroscopy. In addition, the detector system of the SKS can trigger kaon events with good efficiency.

In this chapter, we explained physics interests that motivate the construction of the SKS, particularly about the Λ-hypernuclear spectroscopy by the (π, K) reaction. In the latter half, we describe the design principle and the expected performance of the SKS, and the detector system in detail.

1.2 Physics interests

Λ-hypernuclear spectroscopy by the (π^+, K^+) reaction

A hypernucleus is a bound system of an ordinary nucleus and a few hyperons through the strong interaction. Since a hyperon does not suffer from the Pauli blocking in a nucleus, it can be a good probe to study the interior of a nucleus. It is also a good tool to investigate the hyperon-nucleon interaction. Among various hypernuclei, the Λ-hypernucleus is the easiest to produce experimentally because a Λ hyperon is the lightest hyperon.

A Λ-hypernucleus was first discovered with an emulsion experiment in 1952 [1]. Since then, emulsion experiments had revealed binding energy for many kinds of Λ-hypernuclei. It was found that the potential depth for a Λ hyperon was shallow, $V_\Lambda^0 \sim 30MeV$, compared to that of an ordinary nucleon, $V_N^0 \sim 50MeV$. However those data suffered from their poor statistics. New development started with a pioneering counter experiment by the strangeness-exchange (K^-, π^-) reaction at CERN [2]. A series of (K^-, π^-) experiments had been continued at CERN [3,4,5,6,7,8] and at BNL [9,10], and mass spectra for various Λ-hypernuclei were observed. Particularly in the p-shell hypernuclear spectroscopy for light hypernuclei with mass numbers, $A = 9 \sim 16$, it was found that spin-spin, space-exchange and spin-orbit interactions between a Λ hyperon and a nucleon were much weaker than those between nucleons [11]. The strangeness-exchange (K^-, π^-) reaction is characterized by small momentum transfer compared to the Fermi momentum. Consequently, the reaction preferentially produces substitutional states where a Λ hyperon is replaced with a neutron in the same orbit.

On the other hand, the (π, K) reaction is characterized by large momentum transfer $q > 300MeV/c$ comparable to the Fermi momentum. Accordingly, this reaction selectively produces well separated series of angular momentum stretched states, $[(\text{valence})_n^{-1}, (0s, 0p, ...)_\Lambda]_{j=max}$, of natural parity [12,13]. Therefore the reaction is useful for investigating low lying states of Λ hyperons. Experimentally it was demonstrated first by C.Milner et al. [14] for ${}^{12}_{\Lambda}C$ at BNL. Recently, a series of (π^+, K^+) experiments have been carried out at BNL for various nuclei u to $A = 89$ [15] and for $A = 12, 56$ at KEK [16]. Typical energy resolution of the experiments at BNL was about $3MeV$.

Figure 1.1 shows the mass number dependence of the binding energy for experimental data up to $A = 89$, and theoretical calculations with a Woods-Saxon potential. The similar results are obtained theoretically with other models [17,18,19]. The good correspondence between the experimental data and the calculations shows that a Λ hyperon keeps the single particle nature up to $A = 89$. In other word, a Λ hyperon keeps its identity even in a nucleus to some extent. But it is not clear whether it is ture or not for nuclei heavier than $A = 89$ because the heavier a nucleus is, the more deeply a Λ hyperon can be embedded in it. This would be

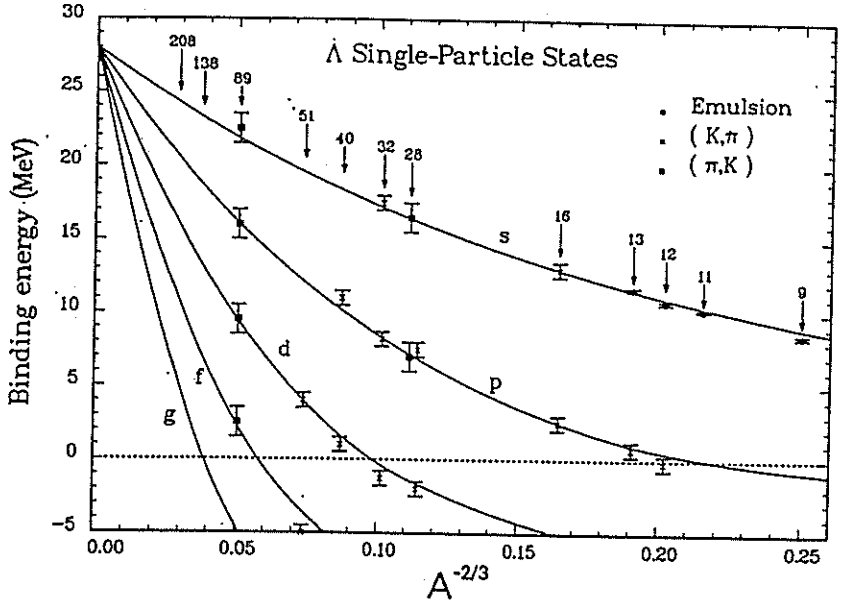

Figure 1.1: Mass number dependence of the binding energy for various Λ orbits. The curves are the theoretical calculations with a Woods-Saxon potential. (from [17])

related to the question how much a nucleon keeps its identity even deeply inside a nucleus. Thus, experimental data for larger mass numbers are expected.

The Λ-hypernuclear spectroscopy of ${}^{208}_{\Lambda}Pb$ by the (π^+, K^+) reaction offers a chance to explore the heavier region. Figure 1.2 shows the calculated mass spectrum for ${}^{208}_{\Lambda}Pb$ with DWIA by T.Motoba et al. [20]. The figure exhibits well separated series of angular momentum stretched states. It is the largest advantage of the (π, K) reaction. The energy spacings of those states are about $4MeV$. If the smearing is not so serious and good energy resolution is in our hand, we can separate those states.

Thus, realization of the good energy resolution of the SKS could provide a good chance to advance the Λ-hypernuclear spectroscopy. Expected experimental yields for the Λ-hypernuclear production by the (π^+, K^+) reaction are estimated for various states in Appendix A.

Σ-hypernuclear spectroscopy by the (π, K) reaction

The Σ-hypernuclei could give interesting information about Σ-N interaction if they actually exist and are clearly observed. But, since there is a *strong* conversion process $\Sigma N \rightarrow \Lambda N$, those states seemed not to exist in the sense that the life time was not large enough compared to a typical time scale of the strong interaction. However unexpectedly narrow width $\leq 10MeV$ was observed experimentally by the inflight $(K^-, \pi^\pm)$ reaction at CERN [21,22,23] and at BNL [24,25]. Various theoretical studies for those states have been done, but they led to only qualitative and controversial conclusions [27]. The ambiguity is mainly because those observed states are not bound states, but in continuum regions. In 1988, an experiment by the $(stopped\, K^-, \pi^-)$ reaction at KEK observed a one bound Σ-hypernuclear state

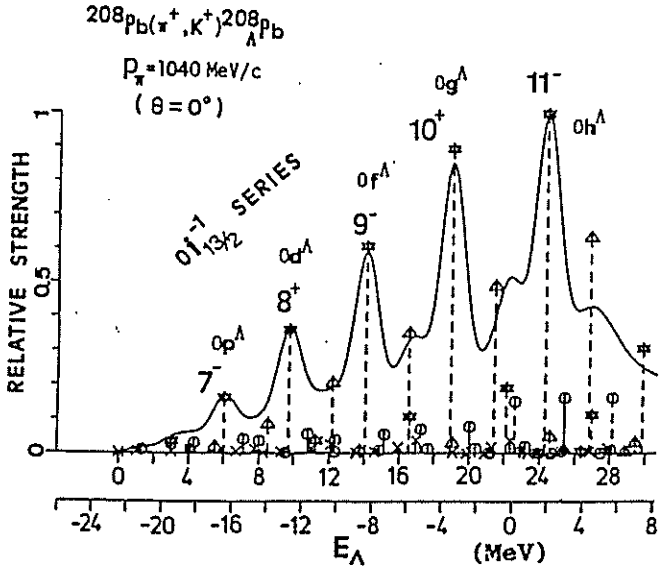

Figure 1.2: DWIA calculations for $^{208}Pb(\pi^+, K^+)^{208}_{\Lambda}Pb$ by T.Motoba et al.[20].

$^{4}_{\Sigma}He$ [26]. Further experiments for bound states are expected now.

H.Bando et al. showed that the (π^-, K^+) reaction would be useful to produce bound Σ^--hypernuclear states [28]. One advantage of this reaction is that it is free from a background of Λ-quasifree production. Another advantage is that the attractive coulomb interaction helps the Σ^- hyperon be bound. Figure 1.3 shows DWIA calculations [28] for $^{28}Si(\pi^-, K^+)^{28}_{\Sigma}Si$ at $p_\pi = 1.5GeV/c$. Also in this case, we can find the merit of the (π, K) reaction, namely, the fact that the reaction produces well separated series of angular momentum stretched states. Note that a spin-orbit pair, $p_{1/2}$ and $p_{3/2}$, is separated. Thus, there would be a direct chance to observe the spin-orbit splitting of the Σ hyperon orbit if the potential parameters used in the calculation are correct. In the calculation, a large spin-orbit force is assumed based on theoretical predictions [29,30,31,32]. Another calculation shows that the cross section takes a maximum value at the beam momentum of $1.25GeV/c$ [33]. Then, the momentum of outgoing kaons is typically $0.85GeV/c$. Hence the momentum range is in a possible region of the SKS.

In Appendix A, expected experimental yields are estimated for $^{28}_{\Sigma^-}Mg$. Though the cross section is much smaller than those for Λ-hypernuclei, they are still in our practical reach. Thus, the large acceptance of 100msr is very important for small cross section measurement like this.

On the other hand, the $A(\pi^+, K^+)_{\Sigma}A$ reaction suffers from a large amount of background \$-quasi free production. The S/N ratio would be of the order of $(0.2\mu b/sr)/(20.\mu b/sr)\sim 1/80$. Hence, without any kinds of coincidence technique which tags Σ production, these experiments would be impossible.

Other physics interests

There are several interesting subjects which can be pursued with the SKS other than the hypernuclear spectroscopy.

The elastic scattering, $(\pi^\pm, \pi^\pm)$ and $(K^\pm, K^\pm)$, is one of those subjects. In the

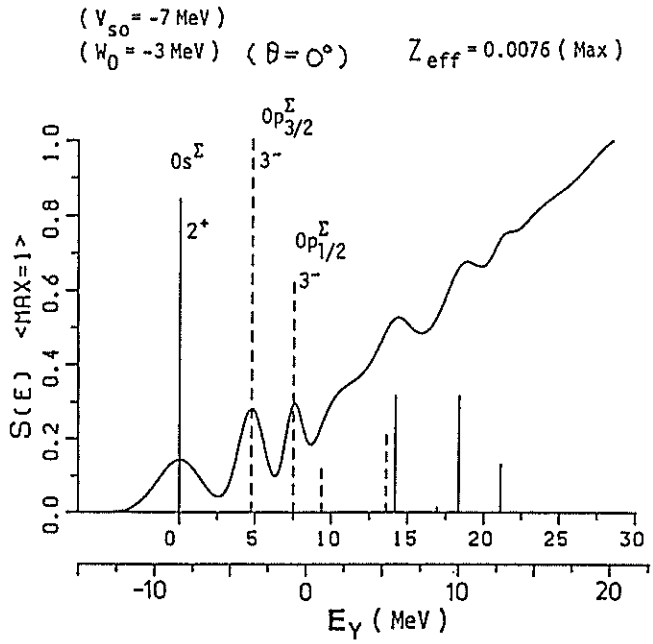

Figure 1.3: Calculated mass spectrum for ${}^{28}Si(\pi^-, K^+)^{28}_{\Sigma}Si$ at $p_\pi = 1.5GeV/c$ with DWIA by H.Bando et al.[27].

momentum region around 1GeV/c, the nuclear reaction is free from the destructive Δ resonance. Hence we could get clear information about the reaction. Actually those experiments were carried out at BNL at the beam momentum of $800MeV/c$ [34,35], and those data stimulated many theorist in this field. With the SKS, we can extend those data up to the momentum of $1.1GeV/c$.

The $(\pi^\pm, \pi^\mp)$ double charge exchange reaction would be also interesting. This reaction has a possibility to investigate the short range nature of the nucleon-nucleon force, because this reaction can occur only by involving two nucleons.

Momentum resolution	0.1%
Maximum momentum	$1.2GeV/c$
Momentum bite	20%
Maximum acceptance	100msr
Bending angle	100°
Flight path length	5m

Table 1.1: Principal design parameters of the SKS.

1.3 The design principle and the expected performance of the SKS

Design of the SKS is optimized for Λ-hypernuclear experiments by the (π^+, K^+) reaction. The good energy resolution better than $2MeV$(FWHM) is one of the most crucial performance for those experiments as described in the previous section. This is achieved with the good momentum resolution of the SKS, 0.1%(FWHM), for outgoing particles, and with the good momentum resolution of the beam line spectrometer, 0.1% (FWHM), for incoming particles. Principal design parameters of the SKS are shown in Table 1.1.

To realize the good momentum resolution of the SKS, the bending angle is taken to be large, that is, about 100° for the central track. To minimize the influence of the multiple scattering, the drift chambers are made as thin as possible, and He-bags are placed between the drift chambers. Furthermore, the magnetic field measurement is to be carried out as accurately as possible (see chapter 3).

The large acceptance of 100msr is very important for good statistics, particularly for small cross section experiments like the hypernuclear spectroscopy. To achieve the large acceptance, the aperture of the magnet is very large as shown in fig. 1.4. The horizontal angular coverage is 30° and the vertical angular coverage is 10°. In addition, the shape of the magnet is a sector, in order that there may be a focussing property in some degree (see fig. 1.4).

A good kaon trigger is also indispensable for studying the (π, K) reaction. The SKS has two layers of silica aerogel Cerenkov counters and a Lucite Cerenkov counter for this end. In addition, the flight path from the target to the last counter is made as short as possible to minimize kaon decay in flight. The life time of the low momentum kaon is so short that about 65% of kaons ($720MeV/c$) decays in 5m.

When we carry out experiments for the Λ-hypernuclear spectroscopy by the (π^+, K^+) reaction, the beam momentum will be set 1050MeV/c where the cross section takes a maximum value. In this case, momentum of the outgoing K meson is about $720MeV/c$. When the SKS magnet is excited to 2.1T at the center of

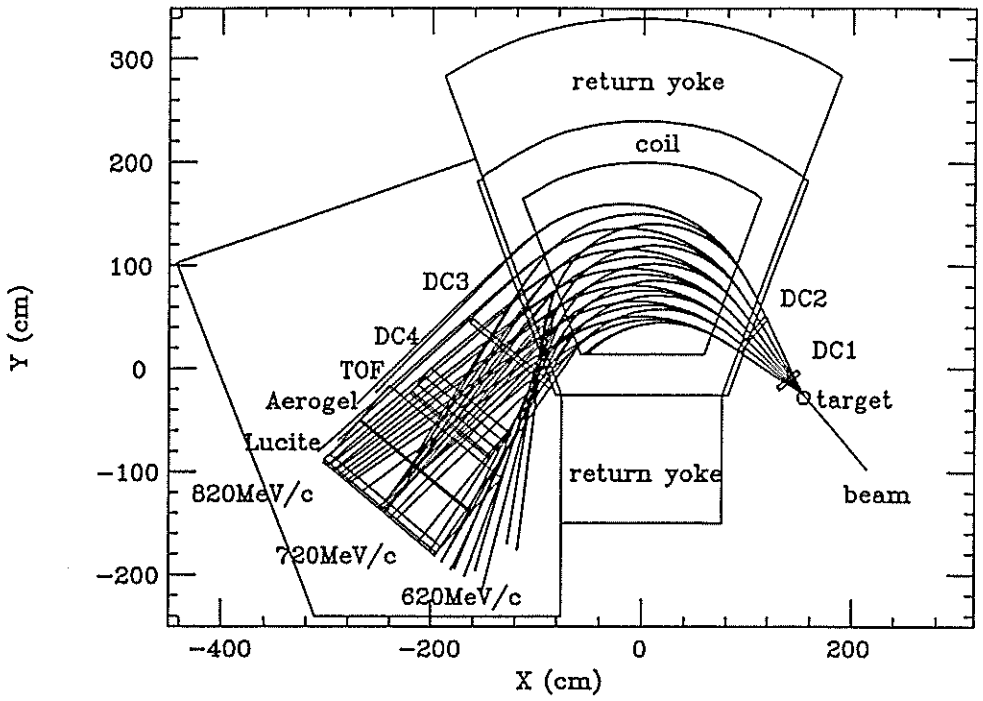

Figure 1.4: A schematic view of the SKS.

the magnet (the 2.1T mode), the acceptance becomes maximum, over 100msr, at this momentum (see fig. 1.5). The many rays shown in fig. 1.4 are calculated for the 2.1T excitation using a magnetic field map calculated with a finite element method.

For experiments with the momentum around 1GeV/c, for example, elastic (π, π) and (K, K) scattering, and for calibration of the beam line spectrometer, the magnet can be excited up to 3T (the 3T mode), where the central track corresponds to about 1.0GeV/c (see fig. 1.5). Figure 1.6 and 1.7 show the calculated magnetic field distribution for the 3T mode and the 2.1T mode. The fringing field is so large in the 3T mode that it is about 300gauss around the silica aerogel Cerenkov counters (see Appendix D).

The KEK-12GeV-PS provides secondary meson beams to the SKS through the K6 beam line, which is under construction in the north counter hall (see fig. 1.8). In the world, now only BNL-AGS and KEK-12GeV-PS can provide secondary meson beams, π, K and $\bar{p}$ in the momentum region around $1GeV/c$. Figure 1.9 compares π beam intensity of KEK, BNL, LAMPF(P^3) and those of two future projects KAON and PILAC. The SKS is an unique apparatus that has the good momentum resolution and the large acceptance simultaneously for this momentum region. Therefore we expect the SKS to offer an indispensable play ground for studying those physics.

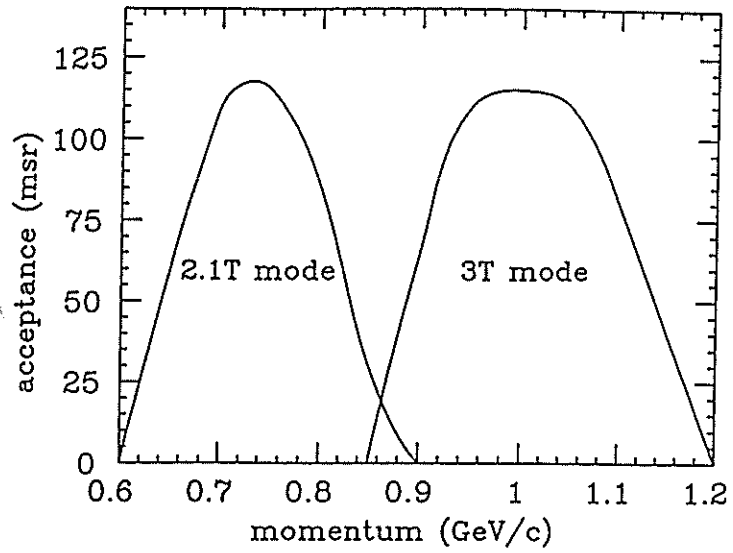

Figure 1.5: The momentum acceptance of the SKS for the 2.1T mode and the 3T mode.

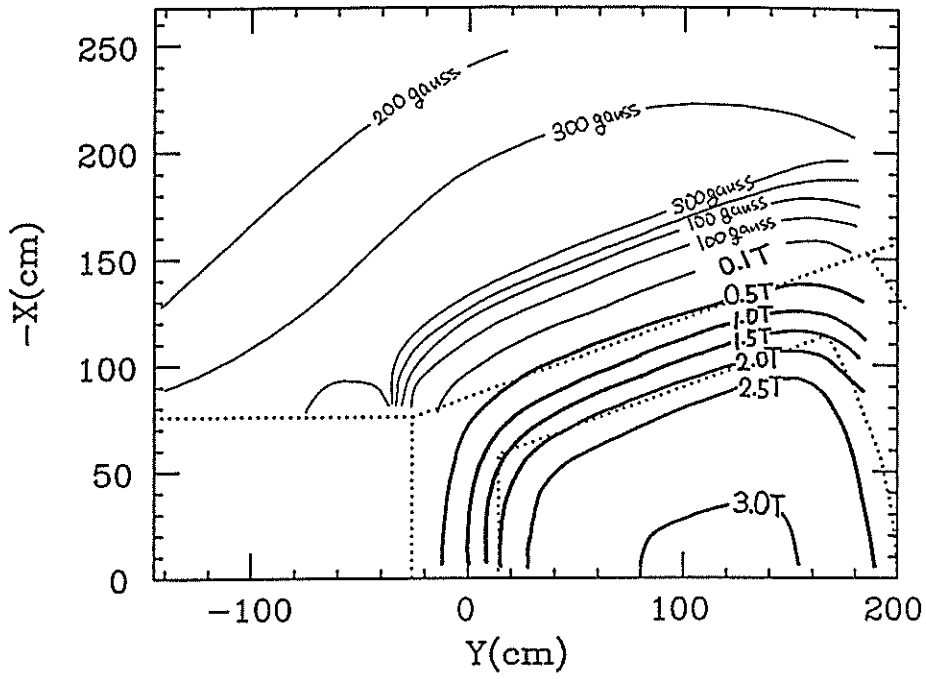

Figure 1.6: The calculated magnetic field distribution for the 3T mode (full excitation) .

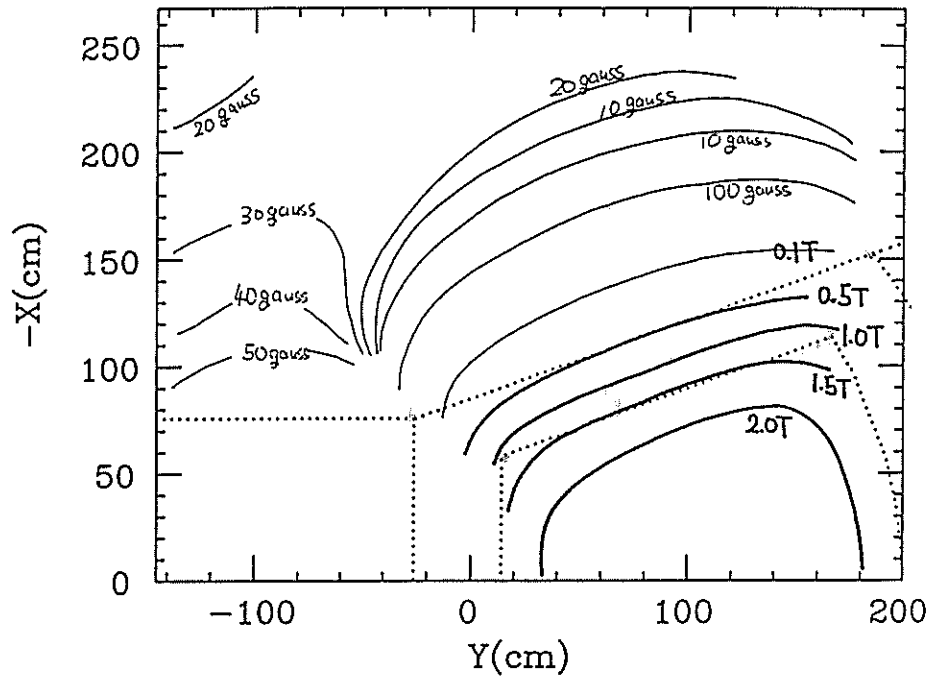

Figure 1.7: The calculated magnetic field distribution for the 2.1T mode .

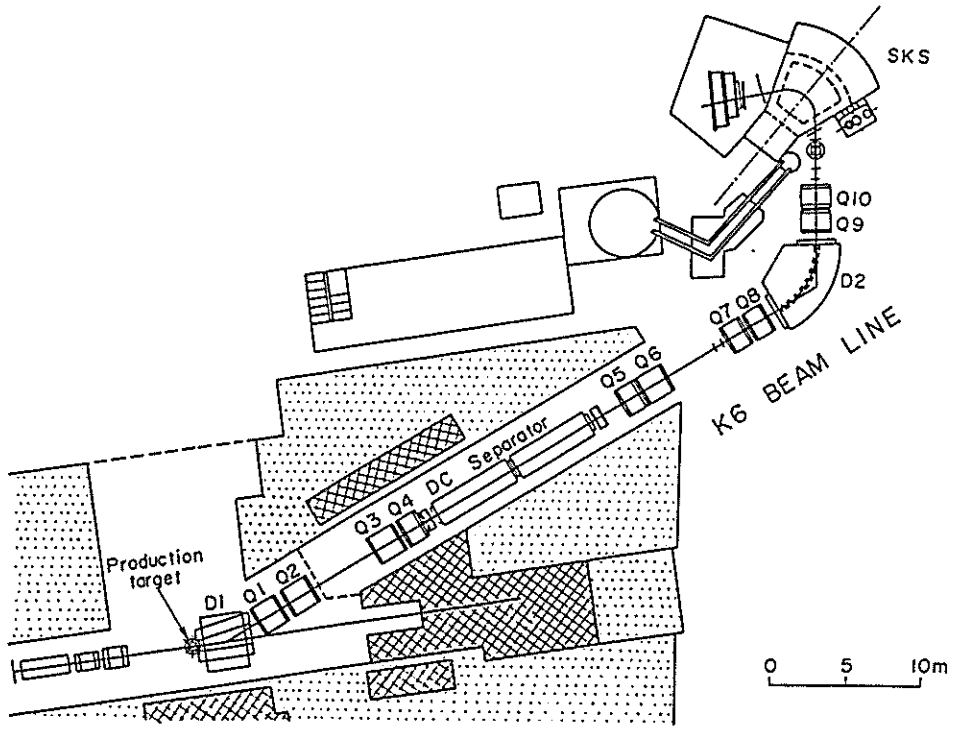

Figure 1.8: A schematic view of the K6 beam line. The QQDQQ system of the beam line spectrometer is named as Q7, Q8, D2, Q9 and Q10 in this figure.

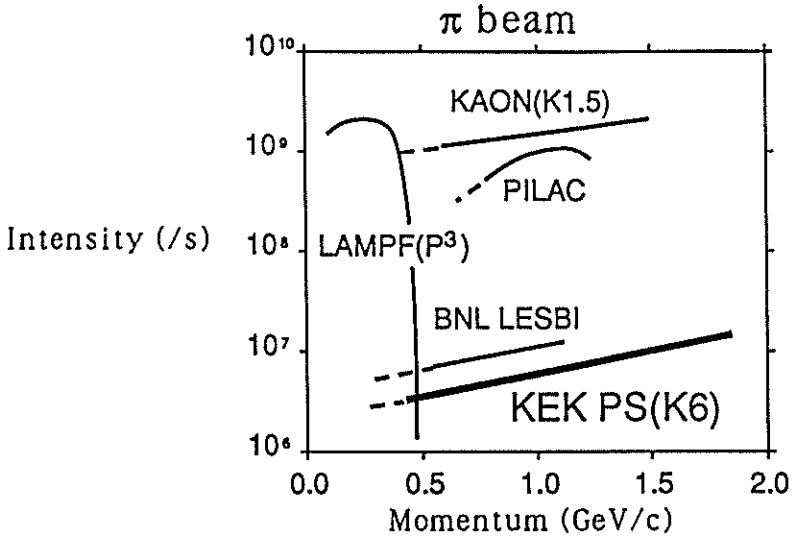

Figure 1.9: The pion beam intensity for some laboratories. Here KAON and PILAC are near future projects.

1.4 Detector system of the SKS

The detector system consists of tracking chambers for the momentum measurement, and trigger counters for particle identification. The former consists of four sets of drift chambers DC1, DC2, DC3 and DC4. The momentum will be determined by solving the equation of motion using the hit positions on the drift chambers and a measured magnetic field map. Since the incident beam goes through DC1 and DC2, they have to endure a high counting rate. On the other hand, DC3 and DC4 are not designed for high rate since incident beam doesn't go through them in the case of Λ-hypernuclear experiments by the (π^+, K^+) reaction. The DC3 and DC4 have relatively large size about 1m × 1m, to match the large acceptance. As will be shown in chapter 3, DC1 and DC4 are more important than DC2 and DC3 for the momentum measurement.

The trigger counters consist of a wall of time-of-flight counter (TOF), two layers of silica aerogel Cerenkov counters and a wall of Lucite Cerenkov counter. The trigger logic is as follows. The TOF counter signals for π, K and p. The silica aerogel Cerenkov counters veto π mesons. The Lucite Cerenkov counter is sensitive only to K and π, but not to p ($< 0.85 GeV/c$). Hence, the combination of three counters can distinguish three kinds of particles (see fig. 1.3). The silica aerogel Cerenkov counters are located between the TOF walls and the Lucite Cerenkov counter because then we can clearly define the area where the veto is required. In the off-line analysis, the time of flight measurement more precisely identifies particles.

The detectors are listed in Table 1.2. Detail descriptions are given in the succeeding subsections.

	effective size (in cm)	performance
Tracking chambers		resolution $\leq$ 200 μm (σ)
DC1	$20^H \times 30^W$	$xx'uu'vv'$
DC2	$20^H \times 41^W$	$xx'uu'$
DC3	$90^H \times 90^W$	X
DC4	$100^H \times 100^W$	XY
Trigger counters		
TOF	$100^H \times 105^W \times 3^T$	resolution $\leq$ 150psec (σ)
Aerogel.1	$120^H \times 140^W \times 42^T$	n=1.055 efficiency $\geq$ 96.5%
Aerogel.2	similar to above	n=1.055 efficiency $\geq$ 96.5%
Lucite.	$140^H \times 140^W \times 3^T$	n=1.49

Table 1.2: The detector system of the SKS.

	π	K	p	momentum
TOF	○	○	○	$> 0.0 GeV/c$
aerogel Cerenkov	○	×	×	$0.4 \sim 1.4 GeV/c$
Lucite Cerenkov	○	○	×	$0.4 \sim 0.85 GeV/c$

Table 1.3: The trigger logic for particle identification. The symbol, "○", represents the fact that the counter signals, and the symbol, "×", the opposite.

1.4.1 Tracking chambers

The high rate drift chambers, DC1 and DC2

The DC1 consists of six layers of drift chamber planes $xx'uu'vv'$ whereas DC2 consists of four layers, $xx'uu'$. The x and x' are vertical (0°) wire planes which are displaced a half cell to each other whereas u and u' (v and v') are 15°(−15°) tilted wire planes. Since the multiple scattering by DC2 influences the momentum resolution of the SKS (refer to chapter 3), the total thickness is made as thin as possible, that is, $L/L_{rad} \simeq 1.2 \times 10^{-3}$ for $xx'uu'$. The L/L_{rad} is the thickness in radiation length. It is generally used as a parameter that characterize the thickness of a medium that causes multiple scattering because the amount of multiple scattering can be estimated with this parameter (see Appendix F). All the wire planes have the same structures as follows. The sense wires are made of Au plated $W(\phi 12.5\mu m)$ and potential wires Au plated $CuBe(\phi 50\mu m)$. The cathode planes are made of $7.5\mu m$ Kapton foils coated with $0.1\mu m$ (1000Å) Al and $0.0015\mu m$ (15Å) Cr on both sides. The chamber gas will be Ar(80%)−Isobutane(C_4H_{10}, 20%) mixture with methylal. The distance of two cathode planes is 4.8mm. For a high counting rate, the drift spacing between a sense wire and a potential wire is made to be small, 2.5mm. These drift chambers keep position resolution of $200\mu m(\sigma)$ for the counting rate up to 10^7 /sec/plane.

DC3

The DC3 measures only the horizontal position. Since the multiple scattering by DC3 also affects the momentum resolution of the SKS, the DC3 is made as thin as possible, that is, $L/L_{rad} \simeq 0.5 \times 10^{-3}$. The effective size is about 90cm × 90cm and the distance between the two windows is about 4.5cm. The wire structure is shown in fig. 1.10. Sense wires are made of Au plated $W(\phi 20\mu m)$ wires and the other wires Au plated $W(\phi 80\mu m)$ wires. We use $Ar(50\%) - ethane(C_2H_6)$ gas mixture. The two windows are made of $25\mu m$ mylar films. The position resolution is expected to be better than $\sigma = 200\mu m$.

DC4

The DC4 consists of two layers of drift chambers DC4X and DC4Y. The two drift chambers have completely the same structure. One is installed vertically and the other horizontally.

The effective size is 1m × 1m and the distance between the two windows is about 10cm. The wire structure is shown in fig. 1.11. One drift cell consists of six sense wires and field shaping wires. Sense wires are made of Au plated $W(\phi 20\mu m)$ wires and the other wires Au plated $W(\phi 80\mu m)$ wires. These sense wires are staggered by $200\mu m$ alternately so that the left right ambiguity can be

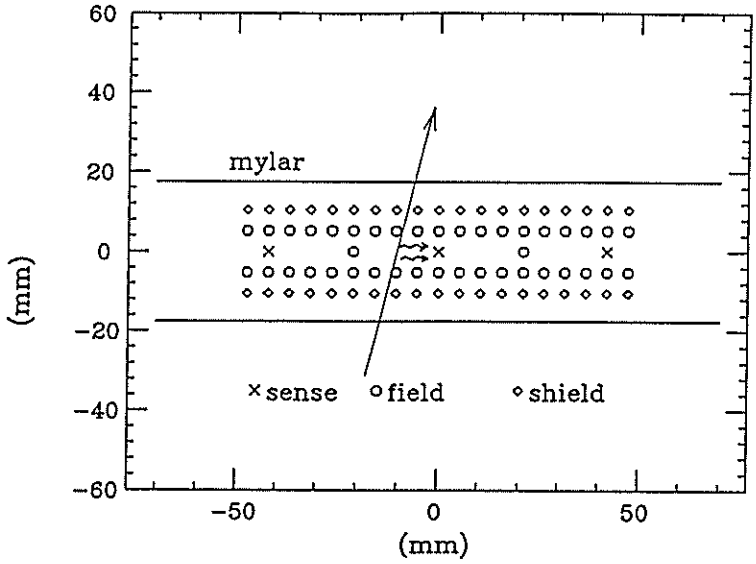

Figure 1.10: The wire structure of DC3.

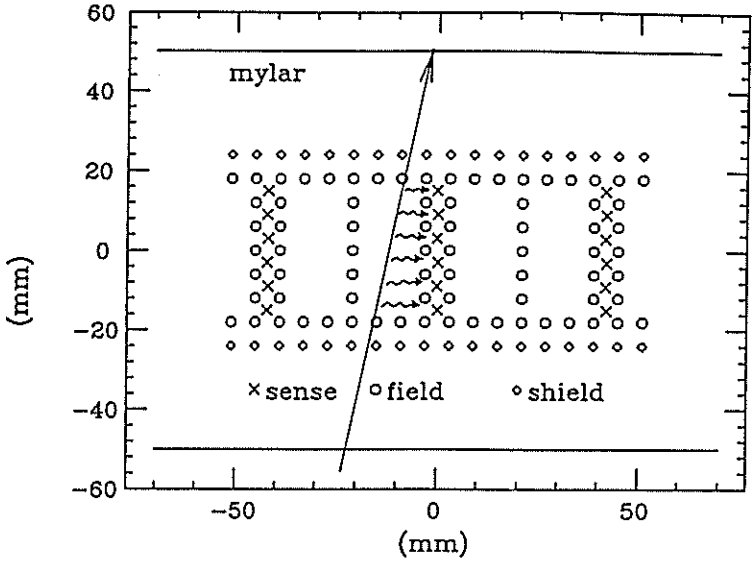

Figure 1.11: The wire structure of DC4X,Y

solved by themselves. The two sense wires at both ends of six sense wires will be ignored as the position information because their position resolution is worse. The windows are made of $25\mu m$ mylar films. We use $Ar(50\%) - ethane(C_2H_6)$ gas mixture. The position resolution is also expected to be better than $200\mu m(\sigma)$.

1.4.2 Trigger counters

TOF wall

The TOF counter is used not only for the time of flight measurement, which precisely identifies particles in the off-line analysis, but also for the particle trigger at the data-taking stage as described at the beginning of this section. The total effective area is about 105cm(height) × 100cm(width). The TOF wall consists of fifteen scintillation counters. The size of one scintillator is 100cm(height) × 7cm(width) × 3cm(thickness). The PMT's(HAMAMATSU H1949) are equipped at both ends of it. The time resolution is expected to be better than $\sigma = 150$ psec.

Silica aerogel Cerenkov counters

The silica aerogel Cerenkov counters play a very crucial role for triggering kaons. We expect pion ($0.7GeV/c$) rejection efficiency to be better than 99.9% for all over the effective area and for any incident angles from $-20°$ to $20°$ with two layers.

One layers has the following structure. The effective area is about 1.2m(height) $\times$ 1.4m(width) with the thickness of 40cm. The refractive index of our silica aerogel is about 1.055. The thickness of silica aerogel is set to be 9cm. The inner surface will be covered with aluminized mylar films. The eighteen PMT's (HAMAMATSU R1584-01 with modification) is equipped on both sides of the counter box (nine PMT's on each side). All the PMT's are protected with double 5mm thickness iron cylinders from the large fringing field from the SKS. The other layer will have a similar structure.

A more detail description is given in chapter 2.

Lucite Cerenkov counter

The Lucite Cerenkov counter is used for discriminating π and K from p for momentum less than 0.85GeV/c at the data-taking stage. To match the large acceptance of the SKS, the total effective area is about 140cm(height) $\times$ 140cm(width). The counter consists of fourteen segments. Each one is 140cm(height) $\times$ 10cm(width) $\times$ 3cm(thickness) in its size. The PMT's (HAMAMATSU H1949) are equipped at both ends of each segment. To get uniform efficiency, the Lucites contain 10ppm wave length shifter (bis-MSB), by which directional Cerenkov photons are diffused.

1.5 The beam line spectrometer

The beam line spectrometer consists of a QQDQQ magnet system, four sets of drift chambers (see fig. 1.8) and trigger counters. The QQDQQ system is so designed that the influence of the multiple scattering by the drift chambers on the momentum resolution is as small as possible. To avoid the multiple scattering by the atmosphere, we will set a vacuum chamber in the D magnet. As a result, we expect the momentum resolution to be better than 0.1%(FWHM) for the momentum around 1GeV/c. We use a dipole magnet that is called KAMAE as the D magnet. Each of the drift chambers has a similar structure as DC1. Trigger counters will consist of a gas Cerenkov counter to veto electron contamination in pion beams and a segmented scintillation counter, which gives the time zero.

Chapter 2

Silica aerogel Cerenkov counters

2.1 Introduction

The special feature of silica aerogel is in its refractive index, which can be set between 1.02 and 1.1 arbitrarily depending how it is produced [36,37,38]. This region of refractive indices is just in between those for gas (typically < 1.002 at 1 atm and room temperature) and liquid (typically > 1.3). Figure 2.1 shows the threshold curves of Cerenkov radiation for various radiators. We can find that silica aerogel is very much useful as a Cerenkov radiator to identify particles for momentum around a few GeV/c.

Silica aerogel has been used in many experiments as a Cerenkov radiator ([39,40,41,42,43,44,45] for relatively larger counters, [46,47,48,49] for smaller counters). Table 2.1 shows principal parameters of those counters of relatively larger size. The words "H"(height), "W"(width), "T"(thickness) and "thickness" (counter box thickness) are defined in fig. 2.2. The $\overline{N_e}$ is the mean photoelectron number produced at the photocathodes of PMT's by the photoelectric effect. It is generally used as a measure of the efficiency of a Cerenkov counter. Those counters were viewed from one side of a counter box with PMT's. Note that, in each case, several counters of the same size were arranged to make a larger effective area.

2.2 Requirements for a pion veto counter of the SKS

For the hypernuclear spectroscopy by the (π, K) reaction, we need a trigger counter to veto π mesons in order to select K mesons in the momentum region around 0.7GeV/c. In general, when one wants to distinguish K mesons from π mesons in this momentum region, liquid N_2 and silica aerogel are candidates for a Cerenkov radiator (see fig 2.1). The largest advantage of liquid N_2 is that it radiates more Cerenkov photons than silica aerogel in a same thickness because of its large refractive index. Its disadvantage is that the windows have to be thick in order to

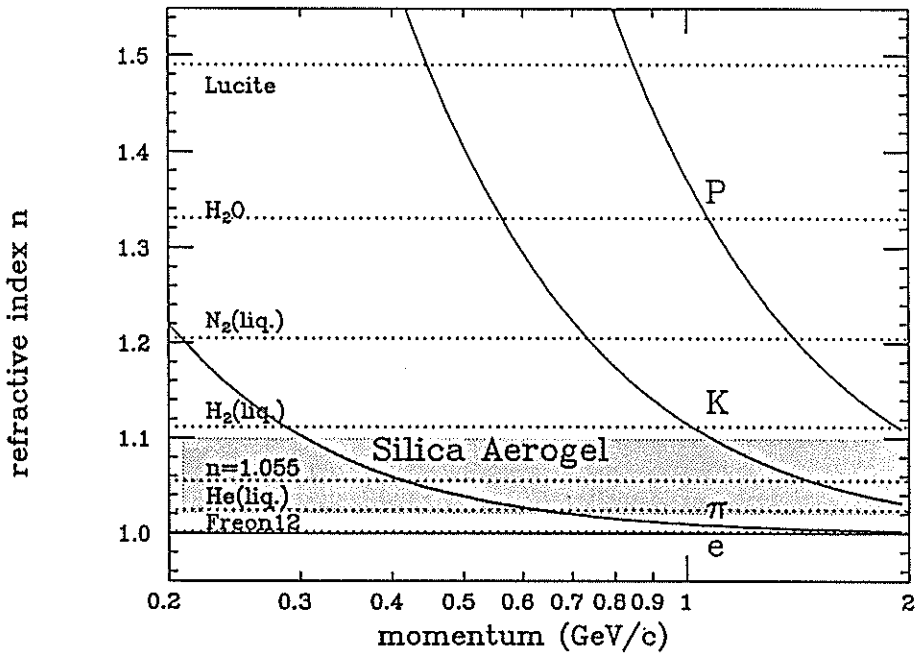

Figure 2.1: The threshold curves of Cerenkov radiation. The shaded area represents the possible range of refractive indices of silica aerogel.

ref.	silica aerogel		box	$\overline{N_e}$	PMT
	size(H × W × T)	n	thickness	($\beta = 1$)	
[39]	$18cm \times 52cm \times 9cm$	1.030	55cm	$3 \sim 6$	RCA8854 (× 2)
[40,41]	$31cm \times 65cm \times 18cm$	1.030	60cm	$4 \sim 6$	RCA8854 (× 5)
[42,43]	$23cm \times 55cm \times 14cm$	1.030	65cm	$8 \sim 14$	RCA8854 (× 2)
[44,45]	$40cm \times 100cm \times 20cm$	1.025	110cm	4	RCA8854 (× 6)
-	$16cm \times 50cm \times 6cm$	1.055	34cm	$4 \sim 6$	HAMAMATSU R1250 (× 1)

Table 2.1: Silica aerogel Cerenkov counters of larger size used in experiments so far. The $\overline{N_e}$ is the mean photoelectron number.

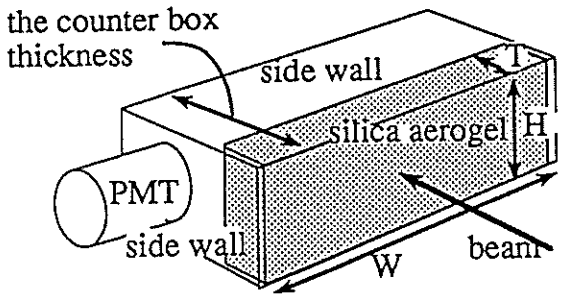

Figure 2.2: The definition of the words "H(height)", "W(width)", "T(thickness)" of the silica aerogel and the "counter box thickness".

keep the heat leak through them small enough. This is a serious problem particularly for a large counter whose effective area is over 1m × 1m. On the other hand, the windows can be made quite thin for a Cerenkov counter with silica aerogel. The disadvantage of silica aerogel is that they must be kept dry (see Appendix E) and that they are fragile. However, they could be overcome with our careful handling and by circulating dry N_2 gas in the counter.

Furthermore, we want to veto π mesons up to 1.2GeV/c for experiments like the elastic $(K^{\pm}, K^{\pm})$ scattering etc. For this momentum region, liquid N_2 is no longer capable of distinguishing K mesons from π mesons. Therefore silica aerogel is the best and unique choice for us as the Cerenkov radiator.

The required pion rejection efficiency will be determined to keep the trigger rate lower than the maximum data-taking rate. From an experience of an experiment that studied the (π^+, K^+) reaction at KEK (PIK E150) [16], we estimated that it would be required to achieve 99.9% pion rejection efficiency.

The effective area must be larger than 1m × 1m to match the large acceptance of the SKS. In addition, the counter box should be as thin as possible so that the flight path in the spectrometer can be short. Since the incident angle varies from $-20°$ to $20°$ (see fig. 1.7), we also need uniformity about the incident angles.

Design principles of the counters

To avoid inefficiency in the vicinity of boundary walls, we decided to adopt one-box-type counters with the large effective area. It is in contrast to the counters listed in Table 2.1, which are all segmented-type as mentioned in section 2.1. In addition, to get good efficiency at the center of the counters, we put photomultiplyer tubes (PMT's) on both sides of them. This is also in contrast to them.

To satisfy the requirement for the efficiency better than 99.9%, we decided to adopt the two layer system. Here the two layer system means that two counters are put side by side so that each particle can go through the two counters. In this case, each counter is required to have efficiency about 96.5%, which corresponds to $\overline{N_e} \sim 4.3$. It is easier to make two counters of better efficiency, 96.5%, than to make one counter of very good efficiency, 99.9%.

Based on the above considerations, we made a prototype counter to get important information for the final designing. The test experiment of the prototype silica aerogel Cerenkov counter is described in detail in the next section. We also developed a Monte Carlo simulation code for silica aerogel Cerenkov counters. Detail description of the Monte Carlo calculation will be given in section 2.4. Using these two kinds of information, we design the final type of the silica aerogel Cerenkov counters of the SKS.

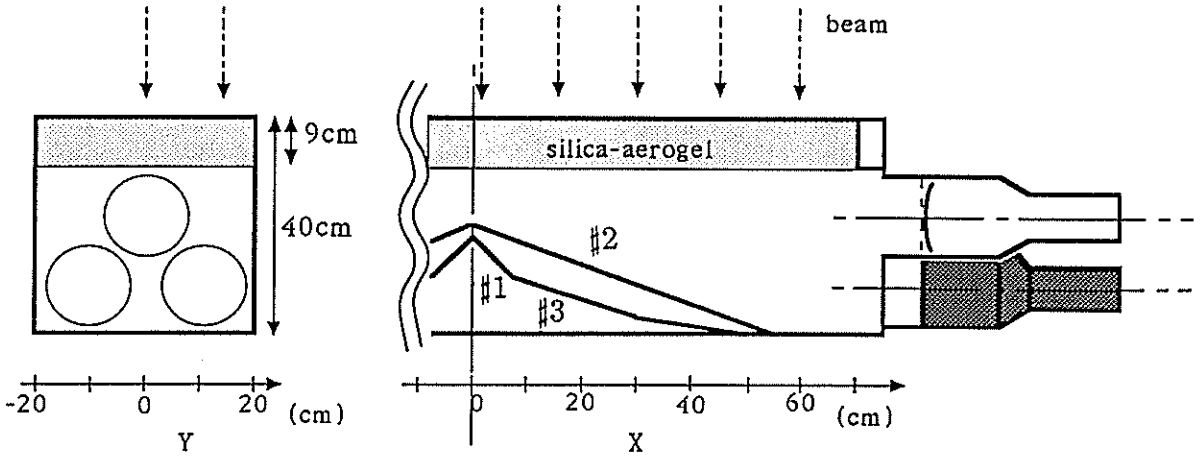

Figure 2.3: A schematic view of the prototype counter. Here only a half is shown because of its symmetry.

2.3 Prototype counter

We made a prototype silica aerogel Cerenkov counter to get crucial information for the final designing. What we want to know with the prototype is as follows.

1)Whether the uniform efficiency over 96.5% is possible or not.

2)What kind of reflectors is good in shape and materials?

In this section, the test experiment of the prototype counter is described in detail.

2.3.1 Details of the prototype counter

Figure 2.3 shows a schematic view of the prototype silica aerogel Cerenkov counter.

The size of the counter box is 40cm(H) × 150cm(W) × 40cm(T). The height of the counter box is about one third of the required height for the SKS. We can estimate the efficiency of the full size counter from that of the small height counter as will be shown in section 2.5.

The ratio of the thickness to the width is very small compared to those for the counters listed in Table 2.1. Naively thinking, when PMT's are equipped on the side of counter box with a certain density, the larger the thickness is, the better efficiency we can expect. This is because of the increase of the ratio, of the number of PMTs to the total area of the inner surfaces. The thickness, 40cm, is chosen based on a result of a preliminary test with cosmic rays.

The effective volume of the silica aerogel is 40cm(H) × 140cm(W) × 9cm(T). This total size is composed of forty-two pieces of silica aerogel. One piece has the size of about 20cm × 20cm × 3cm. These pieces were produced by *the Airglass company* in Sweden. The refractive index was set to be 1.055, which is the highest value easily achieved by the company. These pieces of silica aerogel are arranged

orderly to make the total effective area. The thickness, 9cm, is so chosen that about four mean photoelectrons can be obtained, based on a result of a preliminary test with cosmic rays.

The number of PMT's is six for both sides, three for each side. The PMT's are not put on as dense as possible on the sides of the counter box, since the space for magnetic shields is needed (see Appendix D). The PMT's are 5 inch HAMAMATSU R1584-01 (12cm diameter) with modification on the divider circuit (see Appendix B). The photoelectric windows are made of UV-glass.

Air light guides of 7cm long (not tapered cylinders) are placed right before the PMT's. Their inner surfaces are covered with aluminized mylar films. We have confirmed that the prototype with 15cm long air light guides had almost the same efficiency as that with 7cm long ones by a cosmic ray test.

In general, two kinds of materials are widely used as reflectors; mirrors (aluminized mylar films, etc.) and diffusive papers or paints (white papers or paints etc.). The shape of reflectors is important when mirrors are used whereas it is not for the latter. Therefore, we tested three kinds of reflectors. The first one (♯1) is imitating a parabolic reflector and it is covered with aluminized mylar films. The second one (♯2) is a linear reflector covered with aluminized mylar films. The third one (♯3) is an empty box covered with millipore papers. Here, the millipore paper is a high reflectivity white diffusive paper.

2.3.2 Test experiments

The test experiment was performed using a π^- beam at the T1 beam line of the KEK-12GeV-PS. The momentum is set to be 0.7GeV/c, which is the case for the Λ-hypernuclear experiments by the (π^+, K^+) reaction. The electron contamination was vetoed with a freon12 gas Cerenkov counter, so that the electron contamination in the pion beam is smaller than 0.1%. Two trigger scintillation counters were placed right before and right after the prototype counter. The size of the former one is 2cm × 2cm and the latter 10cm × 10cm. We changed the incident position and the incident direction of the beam in order to examine the uniformity of efficiency. Each data at a certain incident position and at a certain incident angle includes more than ten thousand events.

It should be noted that we can not compare directly our results with the data in Table 2.1 about $\overline{N_e}$ because the β is 0.9806 for the $0.7GeV/c$ pion beam. The mean photoelectron number for $0.7GeV/c$ pions can be converted to that for $\beta = 1$ by multiplying it by $(1 - \frac{1}{1.055^2})/(1 - \frac{1}{1.055^2 0.9806^2}) \simeq 1.55$ (see eq. 2.1).

2.3.3 Results

Figure 2.4 shows the position dependence of $\overline{N_e}$ for the three reflectors. In the case of the aluminized parabolic reflector (♯1), the efficiency sharply peaks at X=0cm

and elsewhere $\overline{N_e}$ is about four. In the case of the aluminized linear reflector (♯2), nearly uniform efficiency of $\overline{N_e} \sim 4$ is obtained. But at X=0cm, efficiency is relatively worse. In the case of the diffusion box (♯3), $\overline{N_e}$ is ranging from 3 to 5 at $X = 0cm \sim 60cm$. The solid lines are the Monte Carlo calculations and they well reproduce the experimental data both in the position dependence and in the difference of the three reflectors. In the next section, various interesting results by the Monte Carlo simulation about the test experiment are exhibited

Figure 2.5 shows the incident angle dependence of $\overline{N_e}$ for the aluminized parabolic reflector (♯1). In all cases, better efficiency is obtained with the non-zero incident angle than with the zero angle. We can find that the increase of the generated photons due to the increase of the thickness, overcomes other effects that decrease the light collection efficiency.

Figure 2.6 shows the Y dependence of $\overline{N_e}$ for the aluminized parabolic reflector (♯1) at X=0cm. This result clearly shows that the efficiency decreases considerably near the side walls of the counter box.

The mean photoelectron number is related to the the efficiency as follows. If the one-photoelectron resolution of PMT's should be infinitely good, the efficiency could be $1 - e^{-\overline{N_e}}$, where $e^{-\overline{N_e}}$ was the probability for no photoelectron generation in the Poisson distribution with the mean value $\overline{N_e}$. But, actually, this is not the case. In the case of finite resolution, the efficiency gets worse than this ideal value, because the tail of the one-photoelectron peak, spreads out below the threshold. Figure 2.7 shows the relation between the $\overline{N_e}$ and the efficiency for the PMT's used in the test experiment.

2.3.4 Conclusions

We can conclude from the test experiment as follows.

1)With this size where the height is 40cm, we can get about $\overline{N_e} = 4$ for all over the effective area and for any incident angles from $-20°$ to $20°$. The mean photoelectron number $\overline{N_e} = 4$ corresponds to the efficiency of about 96%.

2)The aluminized reflectors are better than the diffusive one. For the uniform efficiency, a certain compromise between the aluminized parabolic reflector (♯1) and the aluminized linear reflector (♯2) would be the best.

3)The mean photoelectron number decreases considerably in the vicinity of the side walls.

4)The Monte Carlo simulation well reproduces the experimental data. Hence, the Monte Carlo code can be used for designing the final counters.

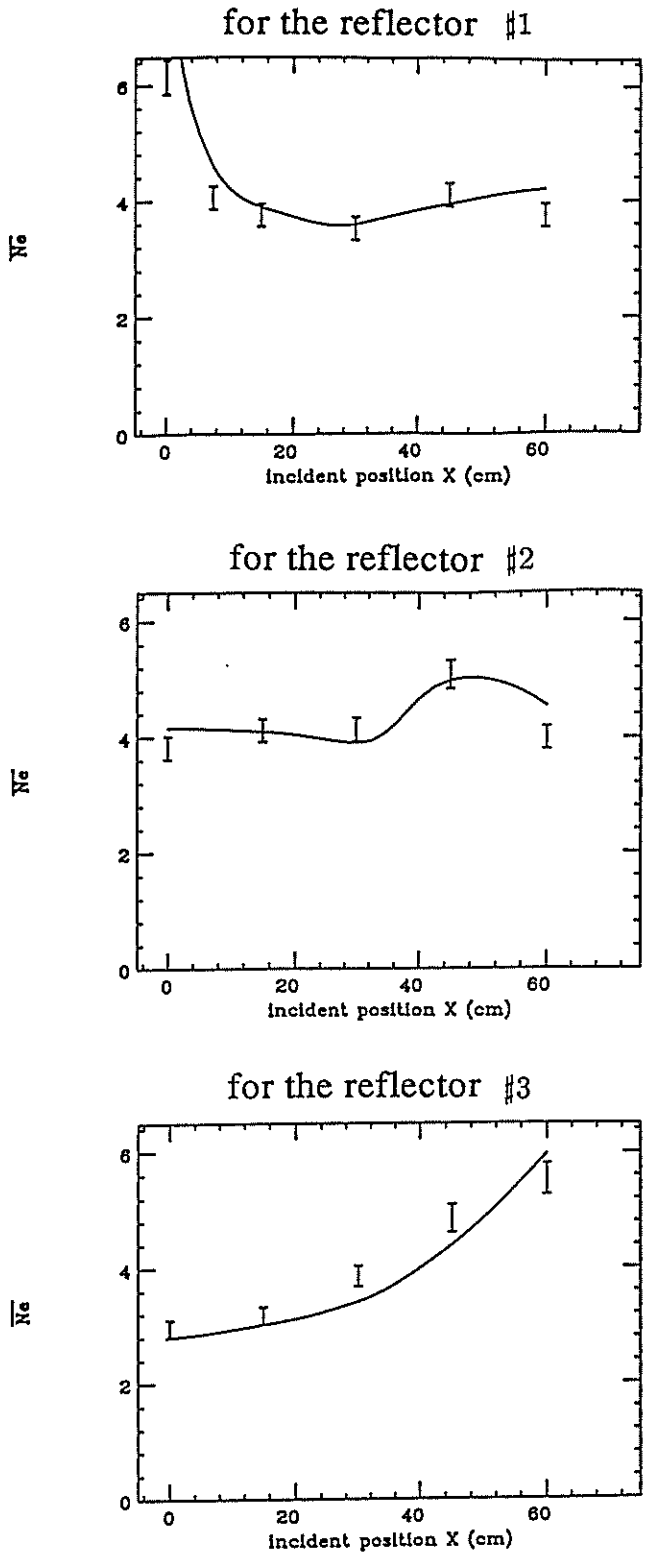

Figure 2.4: The dependence of $\overline{N_e}$ on the incident position X. The bars represent experimental results and the solid lines chain the Monte Carlo calculations.

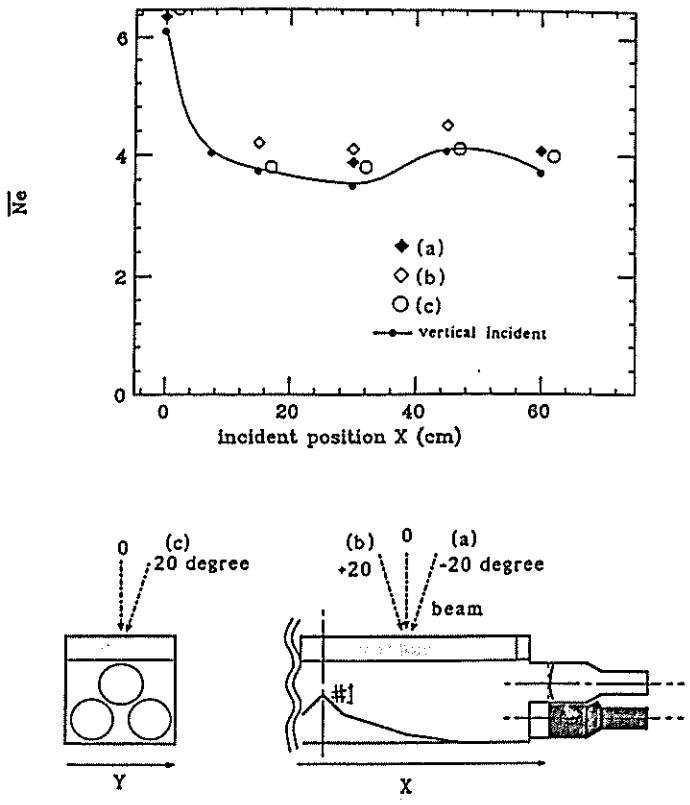

Figure 2.5: The dependence of $\overline{N_e}$ on the incident angle for the reflector ♯1. The solid line is the interpolation of the data for the normal incident.

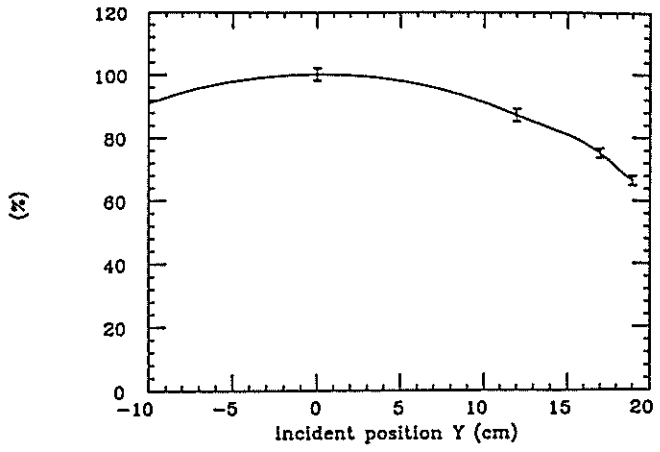

Figure 2.6: The dependence of $\overline{N_e}$ on the incident position Y for the reflector ♯1 at X=0cm. The vertical axis is normalized as the $\overline{N_e}$ to be 100% at Y=0cm.

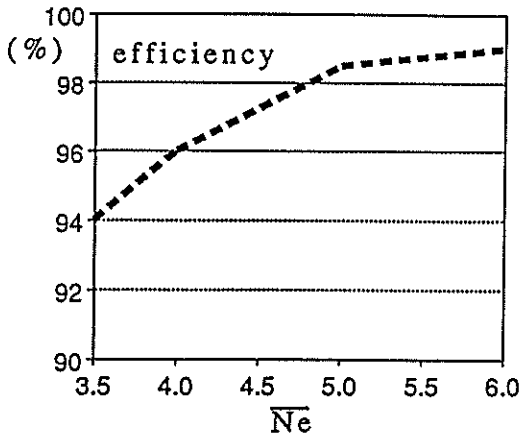

Figure 2.7: The relation between $\overline{N_e}$ and the efficiency for our PMT's.

2.4 Monte Carlo simulation

As shown in the previous section, the Monte Carlo simulation well accounts for the experimental data. In this section, the simulation code is explained in detail. In addition, the Monte Carlo code gives interesting information which is not measurable as will be shown in the latter half of this section. The final design of the silica aerogel Cerenkov counters for the SKS is described in the next section.

2.4.1 Procedure in the simulation

The structure of the simulation program is explained along the propagation of Cerenkov lights. A number of Cerenkov photons emitted, N, is calculated with the following relation,

$$\frac{dN}{dx} = 2\pi\alpha \int_{\lambda_{min}}^{\lambda_{max}} \left(1 - \frac{1}{\beta^2 n^2}\right) \frac{d\lambda}{\lambda^2}, \tag{2.1}$$

where x and n are the thickness and the refractive index of silica aerogel respectively; α is the fine structure constant, λ the wave length of generated photons and β the velocity of incoming particles.

The generated photons propagate in the silica aerogel experiencing scattering and attenuation until getting out of it. The length of straight propagation L until the next scattering is determined with the probability distribution, $exp[-L/L_{scat}(\lambda)]$, where $L_{scat}(\lambda)$ is the scattering length of silica aerogel. The angular distribution is subject to the Thomson scattering,

$$\frac{d\sigma}{d\Omega} \propto \frac{1 + cos^2\theta}{2}, \tag{2.2}$$

where θ is the scattering angle. The attenuation in the silica aerogel is also taken into account with the probability distribution, $exp[-L/L_{att}(\lambda)]$, where $L_{att}(\lambda)$ is the attenuation length of silica aerogel.

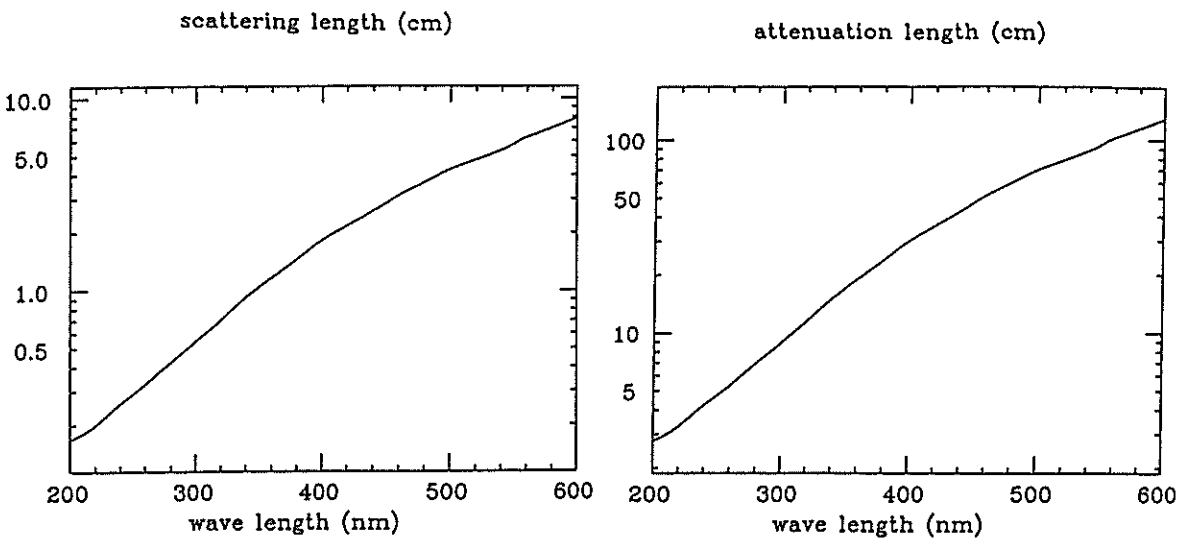

Figure 2.8: The scattering length and the attenuation length of silica aerogel used in the Monte Carlo calculation.

After getting out of the silica aerogel, those photons go to a reflector or a wall and reflected there with a certain reflectivity. The wave length dependence of reflectivity is ignored for simplicity. This is justified because, in general, the reflectivity of aluminized mylar is still better than 80 $\sim$ 90% for wave length larger than 200nm, and most of detected photons have wave length larger than 200nm as will be shown in the next subsection.

In the case of a diffusive paper, the angular distribution of reflection is set to be independent of the incident angles and subjected to the distribution of $cos\theta$, where θ is the angle from the normal direction of the diffusive surface (refer to [50]).

Finally, some of the photons arrive at photocathodes of PMT's and they are converted to photoelectrons with a probability of the quantum efficiency. Thus, we get the N_e counting up the photoelectrons.

Figure 2.8 shows the scattering length and the attenuation length used in the Monte Carlo simulation after the optimization explained below. We estimated the wave length dependence based on measurement of the transmissivity and two references [37,39].

To get the good agreement between the data and the calculations, We optimized three parameters as follows. One is a parameter that represents a diffusive nature of the aluminized mylar films, and the others are overall normalization factors for the attenuation length and for the scattering length. The former stands for the fact that the aluminized mylar films are somewhat crinkled. The diffusive nature is taken into account in the way that a certain percentage of photons are reflected with the diffusive reflection whereas the others with the mirror reflection. The optimized percentage of diffusive reflection is about 30% for the reflector ♯1 and ♯2.

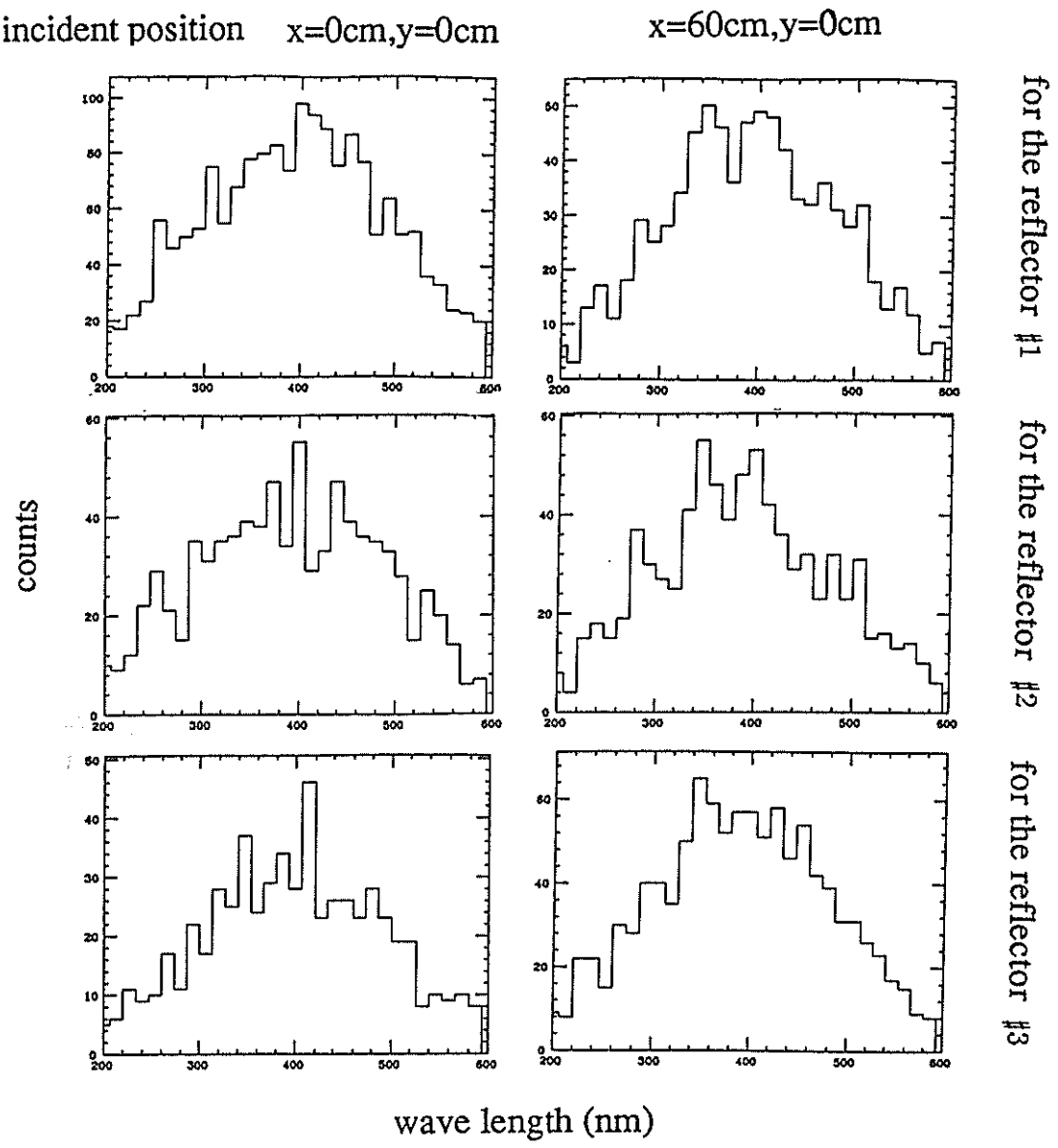

Figure 2.9: Wave length distribution of detected photons.

2.4.2 Simulation for the prototype counter

We selected here eight kinds of results from the Monte Carlo calculations, which are exhibited in the succeeding paragraph in this subsection. All the results are for the six kinds of setup of the prototype counter, those are, six kinds of combination of the three reflectors and the two incident positions X=0,60cm with Y=0cm. The vertical scale, "counts", is normalized for two hundred incident particles.

Figure 2.9 shows wave length distribution of detected photons. The distribution is similar to each other, where it is ranging from 200nm to 600nm. We can recognize clearly from this result that the UV windows of the PMT's are efficient.

Figure 2.10 shows distribution of the number of times of scattering in silica aerogel for detected photons. Most of detected photons experience the scattering

less than twenty times, and mainly less than ten times. We can find the very good efficiency at X=0cm for the reflector ♯1 and at X=60cm for the reflector ♯2 is realized by those photons where the number of times of scattering is less than three times.

Figure 2.11 shows the distribution of path length in the silica aerogel for detected photons. We can find that the photons of path length shorter than 15cm are important. This result is consistent with the previous result.

Figure 2.12 and 2.13 show the first and the last getting out positions from the silica aerogel for detected photons. Here the first and the last getting out positions are the positions where photons get out from the silica aerogel for the first time and the last, respectively. The differences between the two kinds of figures are due to the photons which get into the silica aerogel again and get out of it again.

Figure 2.14 shows distribution of the number of times of reflection on reflectors and walls. Most of detected photons are reflected less than ten times, and mainly less than five times. We can find that the very good efficiency at X=0cm for the reflector ♯1 and at X=60cm for the reflector ♯2 is realized by those photons where the number of times of reflection is very small. These results well agree with the results for the number of times of scattering.

Figure 2.15 shows the distribution of the total path length in the counter box for detected photons. We can find that the very good efficiency at X=0cm for the reflector ♯1 is realized by the photons whose path length is about 90cm. This means those photons go to photocathodes nearly directly.

Figure 2.16 shows hit positions on the back reflector.

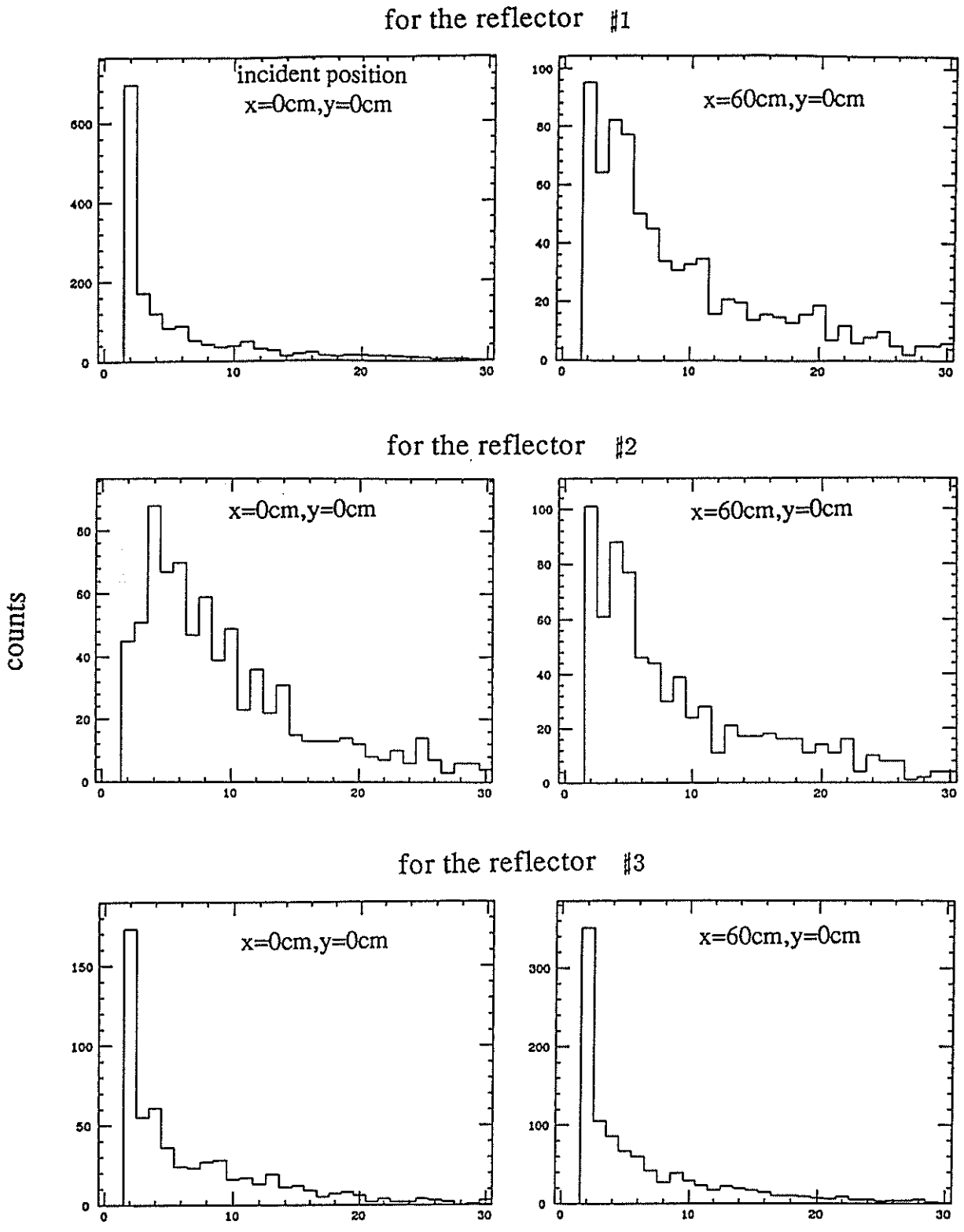

Figure 2.10: Distribution of the number of times of scattering in silica aerogel for detected photons.

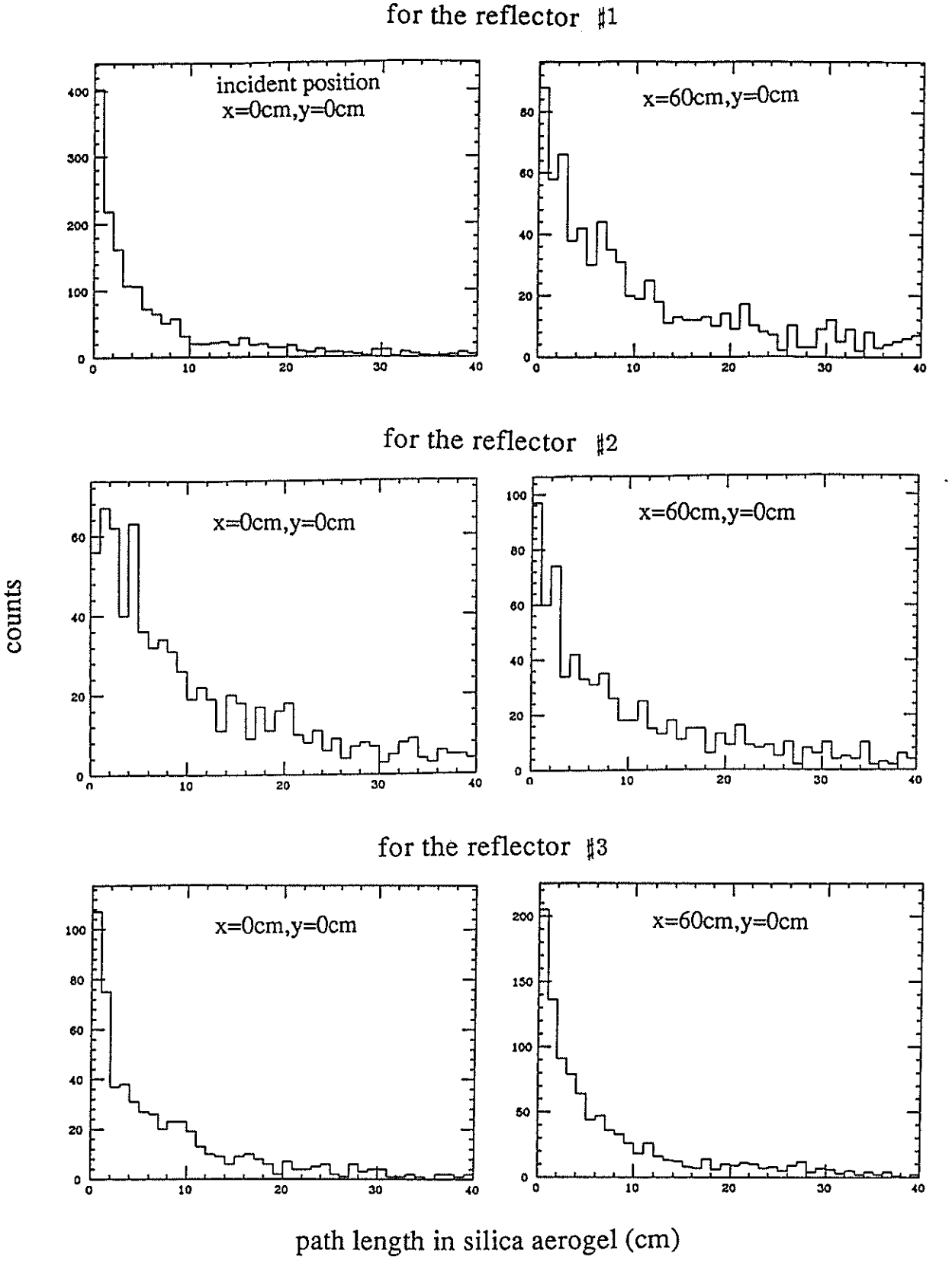

Figure 2.11: Distribution of path length in the silica aerogel of detected photons.

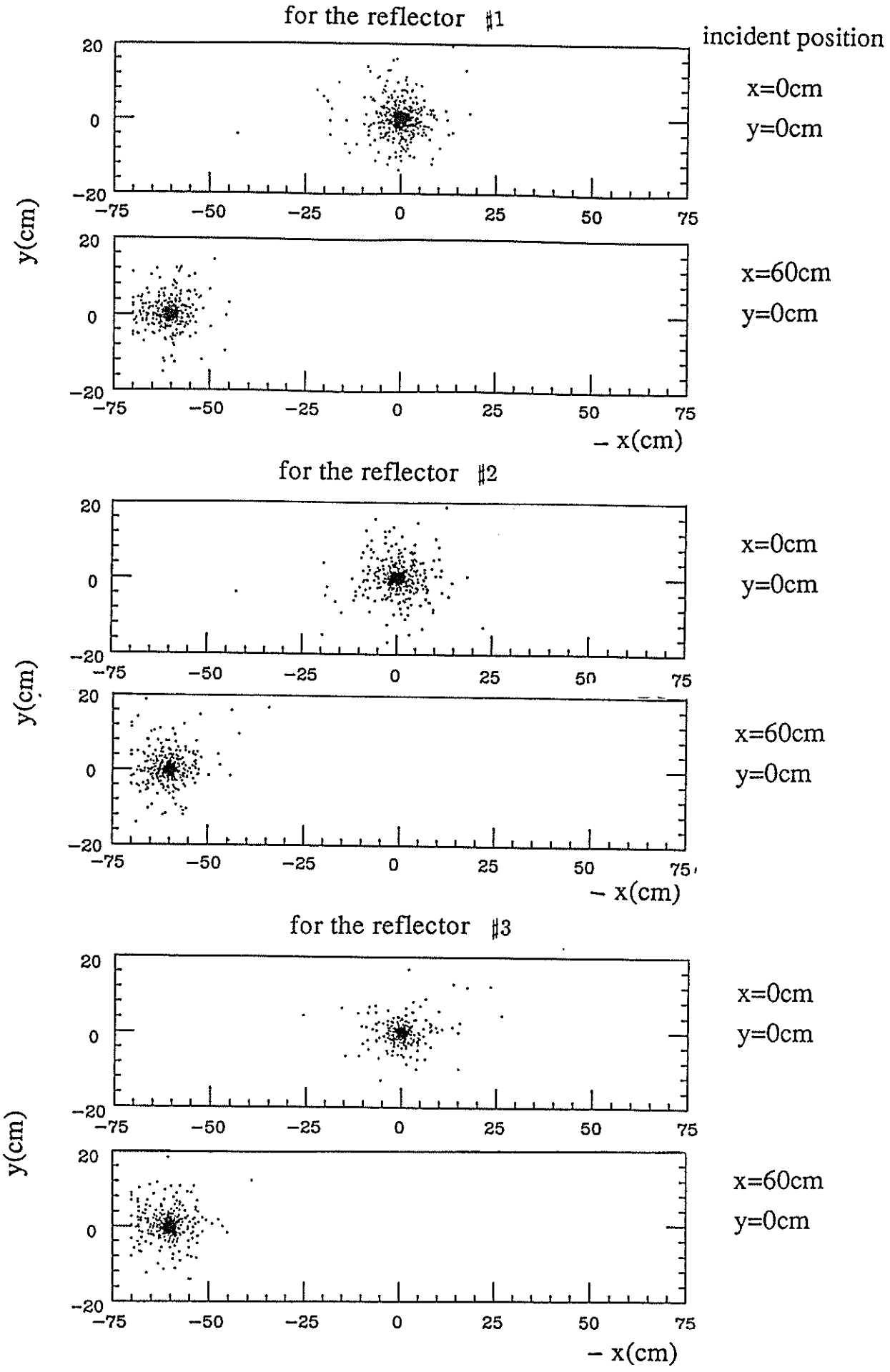

Figure 2.12: The first getting out positions from the silica aerogel of detected photons.

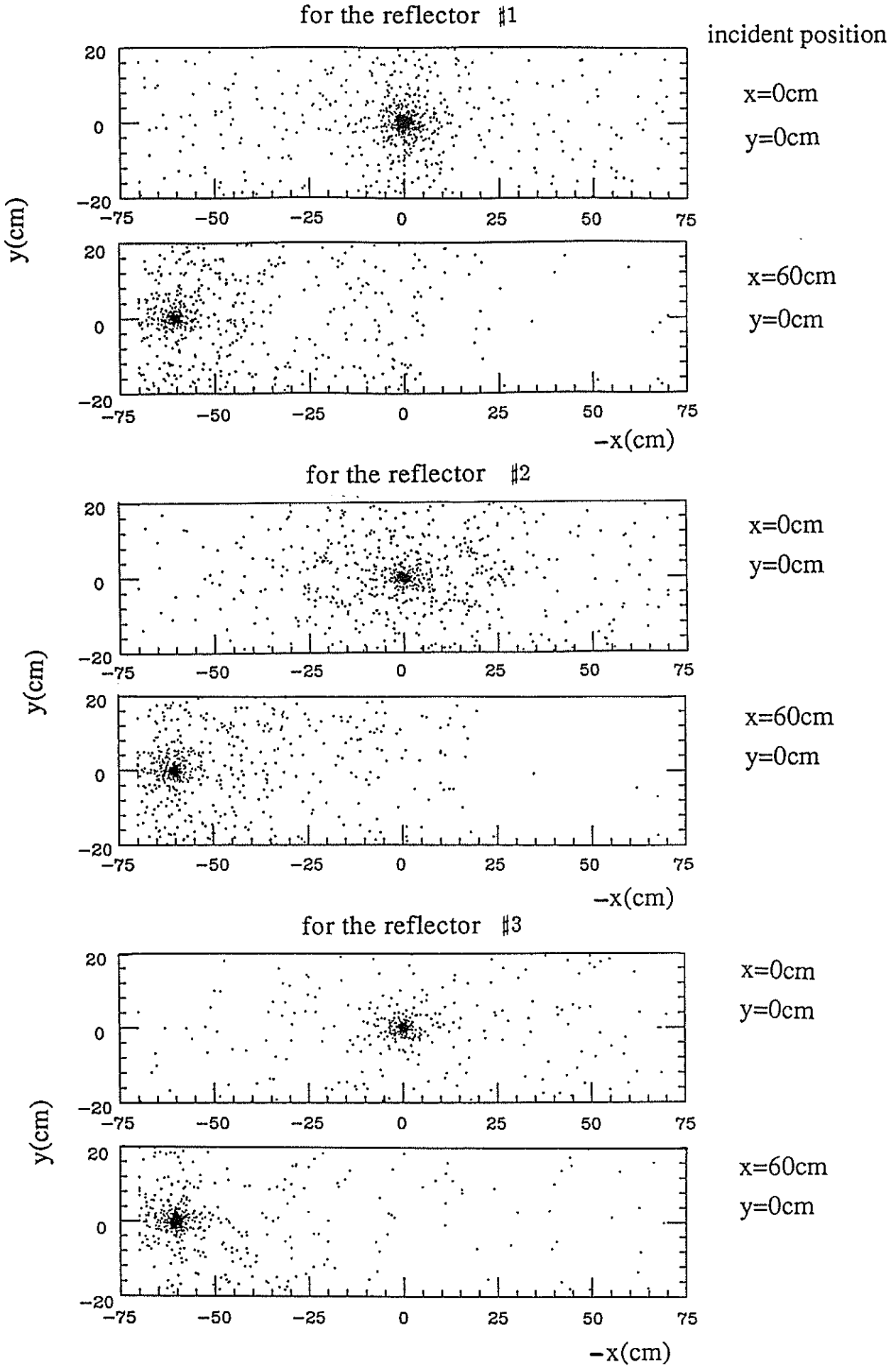

Figure 2.13: The last getting out positions from the silica aerogel of detected photons.

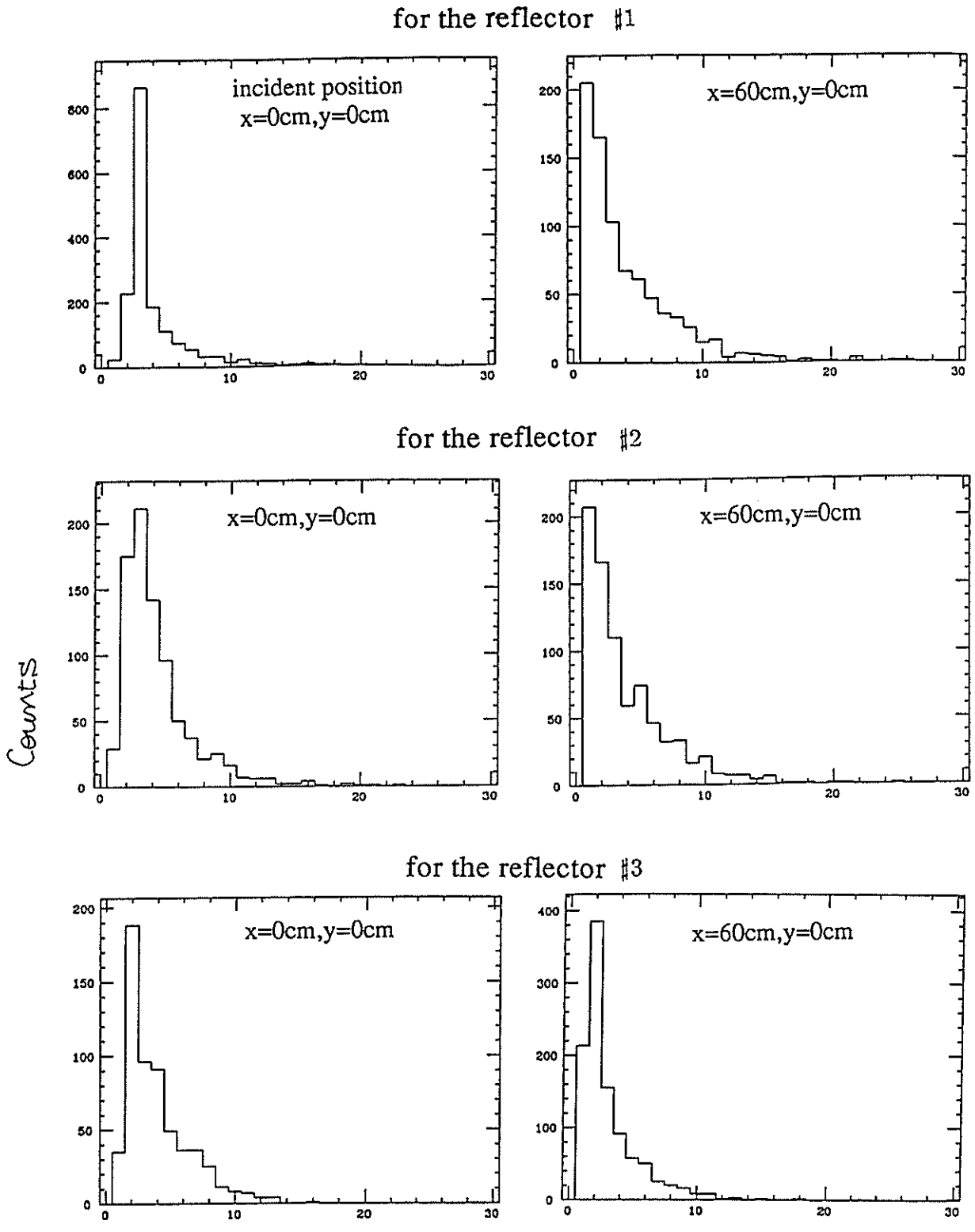

Figure 2.14: Distribution of the number of times of reflection on reflectors and walls for detected photons.

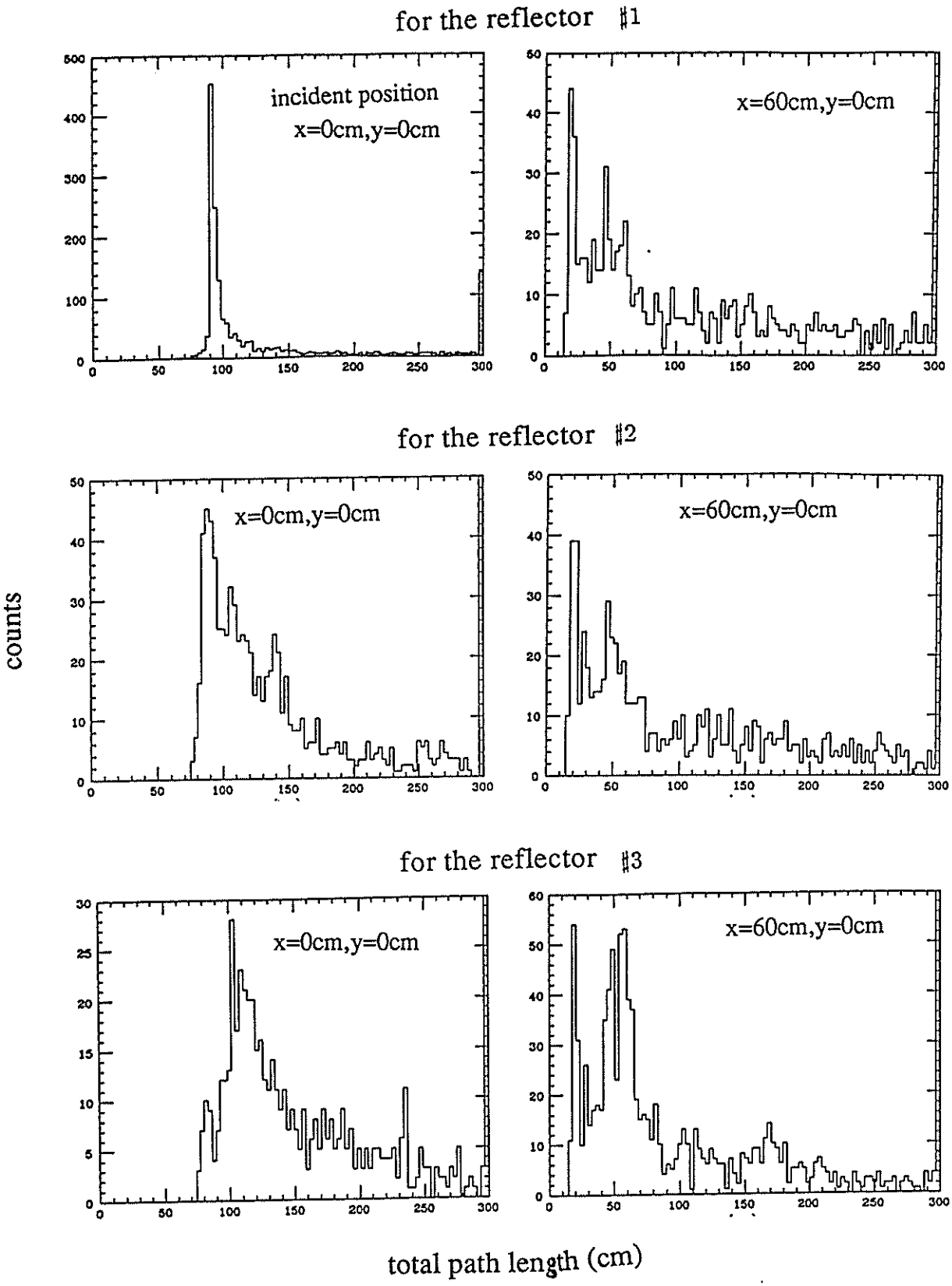

Figure 2.15: Distribution of the total path length in the counter box for detected photons.

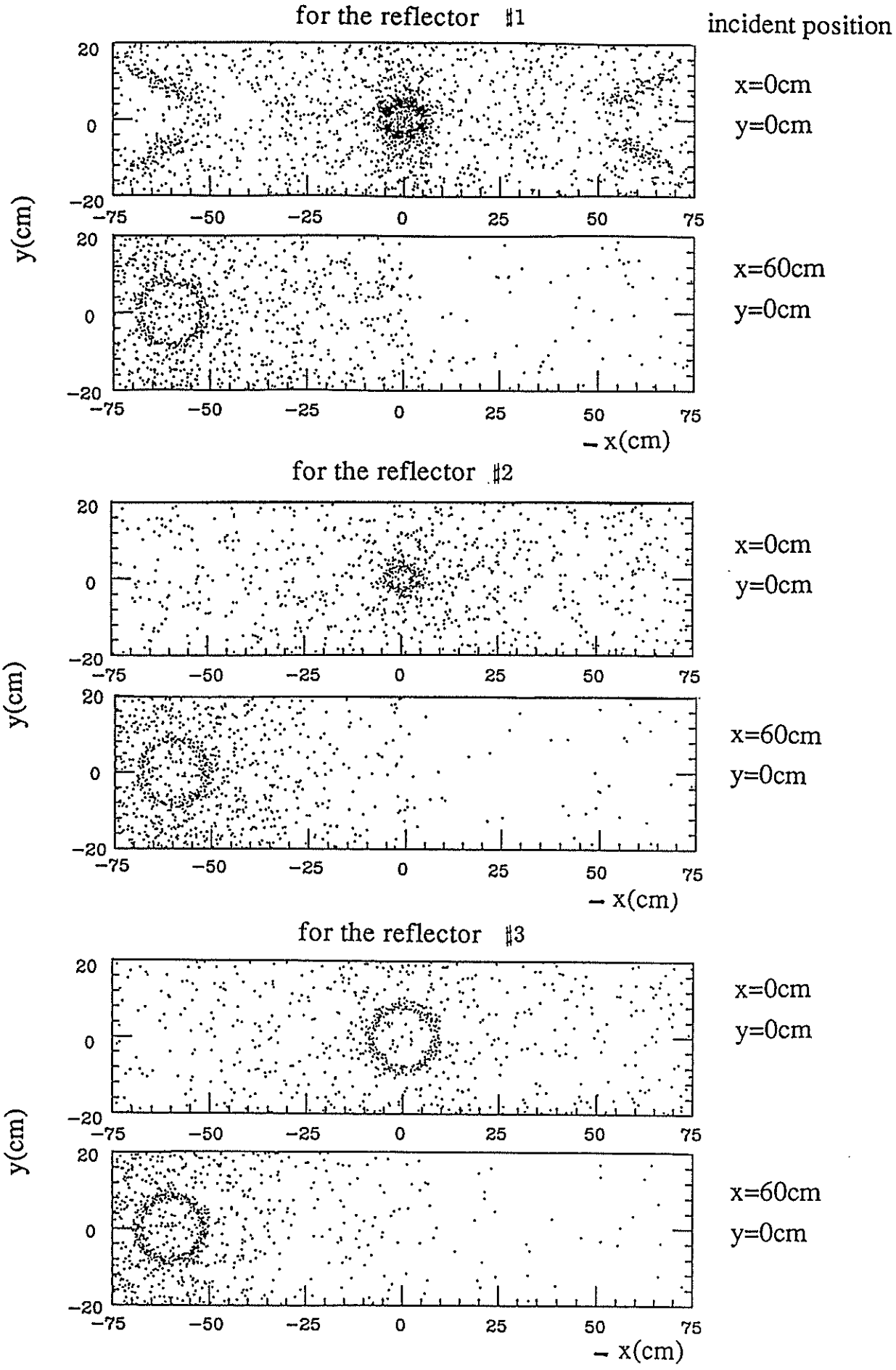

Figure 2.16: Hit positions on the back reflector.

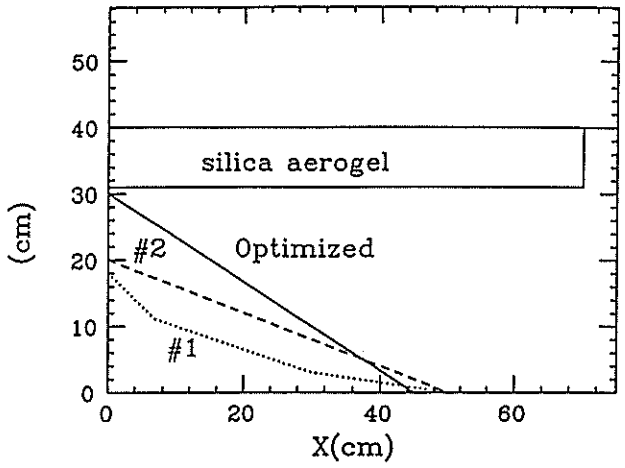

Figure 2.17: A optimized reflector. Here only a half is shown because of its symmetry.

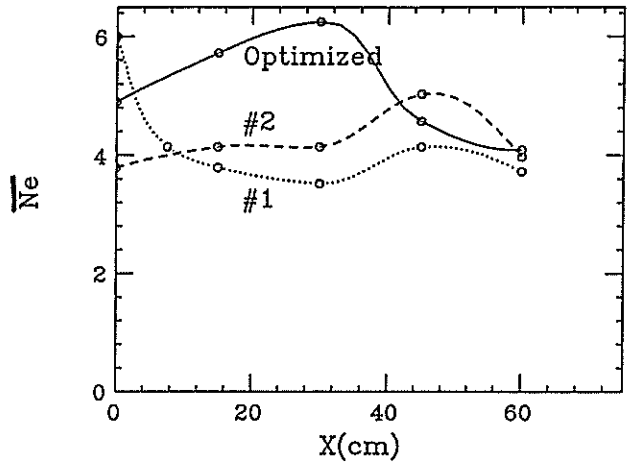

Figure 2.18: The position X dependence of the mean photoelectron number for the optimized reflector. Here only a half is shown because of its symmetry.

2.5 The final design

One conclusion of the test experiment is that a certain compromise between the aluminized parabolic reflector (♯1) and the aluminized linear reflector (♯2) would be the best. We searched a better reflector with the Monte Carlo code. One of the better reflectors we found is shown in fig. 2.17 and the calculated position dependence of the mean photoelectron number is shown in fig. 2.18. Note that the position dependence is sensitive to the shape of the reflector.

Until now, we were concerned with the small height counter, where the height is 40cm though the width is 150cm. But the final counter must have large height over 1m. The difference between the two counters can be considered to be whether there are boundary walls in the counter box or not. Since the walls make the efficiency worse, we can expect better efficiency with the full size counter than with this

box size	145cm(W) × 125cm(H) × 42cm(T)
reflector shape	a linear type
inner surface	aluminized mylar films
silica aerogel size	140cm(W) × 120cm(H) × 9cm(T):total
	20cm (W) × 20cm (H) × 3cm(T):one piece
refractive index	1.055
drying	with N_2 gas
PMT	HAMAMATSU R1584-01 (modified) × 18 (both sides)
air light guide	13.2cm(innerϕ) × 15cm(l)
magnetic shields	1mm$t$ 15.0cm(outerϕ) × 15cm(l):μmetal+
	5mm$t$ 16.5cm(outerϕ) × 47cm(l):iron+
	5mm$t$ 19.2cm(outerϕ) × 47cm(l):iron

Table 2.2: Principal design parameters of one of the final silica aerogel Cerenkov counters of the SKS.

small height counter. In fact, the Monte Carlo simulation showed the increase of the mean photoelectron number was larger than 10% on average.

Based on the conclusions of the test experiment and the above considerations, and also on the results of the magnetic shield test (see Appendix D), we have designed a silica aerogel Cerenkov counter for the SKS. It is now under construction. Important design parameters are summarized in Table 2.2. We expect the efficiency to be well better than 96.5% ($\overline{N_e} = 4.3$). The other counter will have a similar structure. Therefore, in final, we can expect the efficiency better than 99.9% with the two layers, for all over the effective area and for any incident angles, $-20° \sim 20°$ for $0.7GeV/c$ pions.

Chapter 3

Resolution study of the SKS

3.1 Introduction

One of the most important performance of the SKS is its good momentum resolution of 0.1%(FWHM) for the momentum around $1GeV/c$. Momentum of a particle is determined by solving the equation of motion using hit positions on the tracking drift chambers and a measured magnetic field map. In this case, the following factors influence the momentum measurement;

1)position measurement errors with the drift chambers,

2)multiple scattering through the particle trajectory,

3)inaccuracy of the magnetic field map.

In the first half of this chapter, three effects are estimated with a Monte Carlo simulation.

In addition to the SKS itself, other factors must be taken into account in order to get good energy resolution in final; the momentum resolution of the beam line spectrometer, which analyzes the momentum of incoming particles to the target, and energy loss fluctuation in the target. In the latter half of this chapter, experimental energy resolution is estimated taking the Λ-hypernuclear experiment by the (π^+, K^+) reaction as an example.

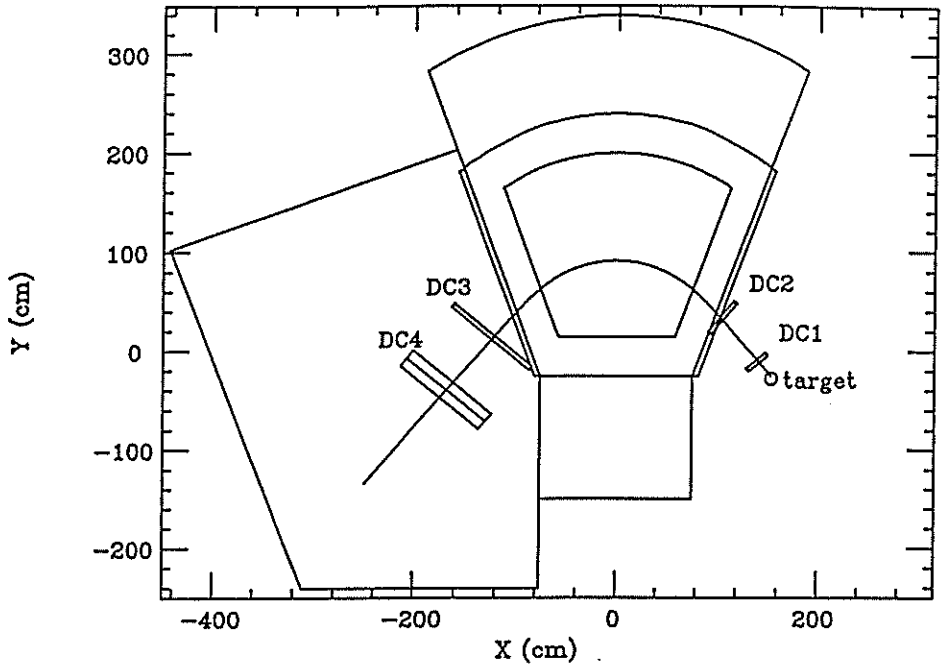

Figure 3.1: Locations of the drift chambers and the target. The track represents the central track mentioned in the text.

3.2 Momentum resolution of the SKS

3.2.1 Simulation procedure

The procedure consists of a event generation process that calculates hit positions on the drift chambers, and a momentum reconstruction process using the hit positions.

Events are generated from the target with uniform angular distribution and with uniform momentum distribution from $620 MeV/c$ to $820 MeV/c$. Tracks are calculated by solving the equation of motion with the Runge Kutta method using the calculated field map for the 2.1T mode. Here, multiple scattering by the drift chambers etc. are taken into account. When a particle goes through the magnet and all the drift chambers, the event is recorded and is subjected to the momentum reconstruction process.

Position detectors consist of four sets of the drift chambers DC1, DC2, DC3 and DC4. Although DC1, DC2 and DC4 have several independent wire planes as described in chapter 1, they are treated in the simulation as single plane position detectors that measure the horizontal and the vertical position simultaneously. We call the horizontal position on the planes "X" and the vertical position "Y". Hence, the information of the hit positions consist of seven variables, those are, DC1X, DC1Y, DC2X, DC2Y, DC3, DC4X and DC4Y. Locations of those drift chambers are shown in fig. 3.1.

The momentum reconstruction process is no other than the derivation process of the five parameters; magnitude of the momentum, its direction and position at the first tracking chamber. The process is as follows.

1)Initial values for the five parameters are roughly estimated using the hit

positions. In the present case, the initial direction of momentum was guessed with DC1X,Y and DC2X,Y and the initial momentum was arbitrarily chosen.

2)With this initial condition, the equations of motion are solved using the magnetic field map. Then all the hit positions on the drift chambers are calculated.

3)The χ^2 is calculated for the differences of the hit positions between data and the calculated values.

4)With a small variation of only one of the five parameters from the initial values, the ray-tracing and calculation of χ^2 are iterated five times for the five parameters.

5)Using those six kinds of values of the χ^2, the next guess for the five parameters are derived. In this derivation, we used a linear approximation explained in [52].

6)These process are repeated until a criteria, for example to χ^2, is valid (see below).

To avoid "the five times iteration" in the process 4), we employed a fast calculation method [51], where "the five times iteration" is omitted by calculating those hit positions simultaneously in the process 2) and 3). In the present case, this method made the CPU time much less than the half.

The χ^2 is calculated with

$$\chi^2 = \sum_{i=1}^{7} \delta_i^2 \times weight_i, \tag{3.1}$$

$$weight_i = \frac{1}{\sigma_i^2} (i = 1 \sim 7) \tag{3.2}$$

where δ_i is the difference of the hit positions and σ_i is the position resolution of the drift chambers; i corresponds to the seven kinds of position information. The criterion for the convergence of the momentum reconstruction process was set to be $\chi^2 \leq 10^{-2}$ and $\Delta\chi^2 \leq 10^{-6}$. The iteration was also stopped when it was over twenty times.

3.2.2 Position measurement errors with the drift chambers

Position measurement errors with the drift chambers can be separated into two parts; one is the intrinsic position resolution of the drift chambers, and the other is inaccuracy of positions of the drift chambers themselves.

Estimated momentum resolution is shown in fig. 3.2 as a function of drift chamber resolution. The momentum resolution increases almost linearly as the chamber resolution σ increases. We can find that the Y components have less influence on the momentum resolution. It is reasonable from the fact that the momentum is mainly determined from the large vending angle in the horizontal plane because the main component of the magnetic field is the vertical one. The DC1X

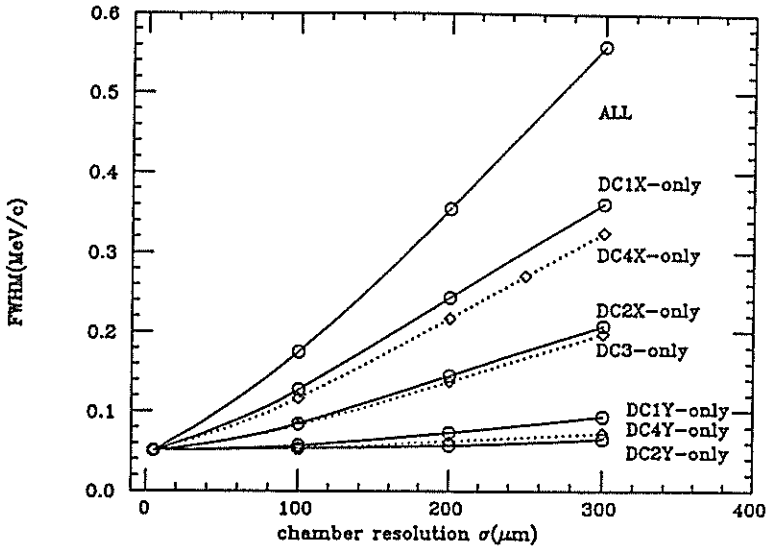

Figure 3.2: Momentum resolution with variation of each drift chamber's resolution without the multiple scattering. Here, for the case of DC1Y and DC2Y, the σ stands for the $4 \times \sigma$ considering the worse resolution.

and DC4X, DC2X and DC3 have similar effect, respectively, which is natural from the symmetrical point of view.

The total influence of all the drift chamber resolution is shown as the curve named "All" in fig. 3.2. Since the position resolution σ can be better than 200 μm, we can expect the momentum resolution to be better than $0.35 MeV/c$. A simple superposition well agrees with "All" as follows. Momentum resolution (FWHM) is about 0.22, 0.22, 0.14 and $0.14 MeV/c$ for DC1X, DC4X, DC2X and DC3 respectively and the superposition is $\sqrt{0.22^2 + 0.22^2 + 0.14^2 + 0.14^2} \approx 0.37 MeV/c$.

Although it is unnatural that the momentum resolution is not zero (FWHM) when σ is zero, it is because of the calculation error in the momentum reconstruction process. We have confirmed that, when the criterion to the χ^2 was set to be more strict and the step size in the Runge-Kutta method was set to be smaller, the σ approached to zero.

Figure 3.3 (a), (b) and (c) show the effect of inaccuracy of the drift chamber positions themselves. The Y component has very small effect also here. Assuming the accuracy is better than $200 \mu m$, the momentum resolution is expected to be better than $\sqrt{0.15^2 \times 2 + 0.2^2 \times 2} \approx 0.35 MeV/c$ (FWHM).

These results are intuitively understandable with a simple calculation. For example, on the drift chamber DC4, the ratio of the momentum range to the corresponding width of the drift chamber is $(200 MeV/c)/(100 cm) \sim (200 MeV/c)/(50 cm)$ (see fig. 1.4). Hence, the position displacement of DC4 in the X direction of 500 μm should produce the momentum shift about $0.1 \sim 0.2 MeV/c$. This value agrees with the Monte Carlo results shown in fig. 3.3(b). These position errors are related to not only the momentum shift as shown in (b), but also the

item	total L/L_{rad}	thickness	effective L_{rad}
DC1	1.79×10^{-3}	$5.4cm$	$2990cm$
DC2	1.18×10^{-3}	$4.2cm$	$2910cm$
DC3	0.53×10^{-3}	$5.0cm$	$9430cm$
DC4X	1.05×10^{-3}	$10.0cm$	$9520cm$
DC4Y	1.05×10^{-3}	$10.0cm$	$9520cm$
He	—	—	$546000cm$
Air	—	—	$29200cm$

Table 3.1: The effective radiation length used in the Monte Carlo calculation.

momentum resolution of the order of $0.1MeV/c$(FWHM) as shown in (c). This dispersion would arise from the fact that the SKS has the large acceptance.

3.2.3 Multiple scattering

The multiple scattering effect is shown in fig. 3.4. In the calculation, the effective mean radiation length was used for each drift chamber, which is shown in fig. 3.1. Here the effective mean radiation length is the length obtained by averaging all the radiation length of wires, mylar or kapton films and gas. Since the position resolution is expected to be better than 200 μm (σ), the momentum resolution should be smaller than $0.4MeV/c$ (FWHM) including the multiple scattering. The figure also shows that the atmosphere makes the momentum resolution considerably worse. Hence, it is vital that He-bags are set between the drift chambers.

Figure 3.5 shows the effect of each drift chamber's multiple scattering as a function of L/L_{rad}. Note that the L/L_{rad} is a good measure of the thickness of a medium that causes multiple scattering (see Appendix F). The DC2 has the largest effect to the momentum resolution. The multiple scattering in DC1 produces no effect. This is because DC1 is located at the end of the drift chamber system. The same is true for DC4.

3.2.4 Inaccuracy of the magnetic field map

We will measure the magnetic field with three Hall probes installed on the instrument for magnetic field measurement. From the structure of the instrument, inaccuracy is expected to be mainly about overall distortion of the structure and probe direction. Therefore, we classify the inaccuracy to three kinds of error; overall parallel displacement of the magnetic field map, the overall inclination of the map and the tilt of $\vec{B}$ at each point.

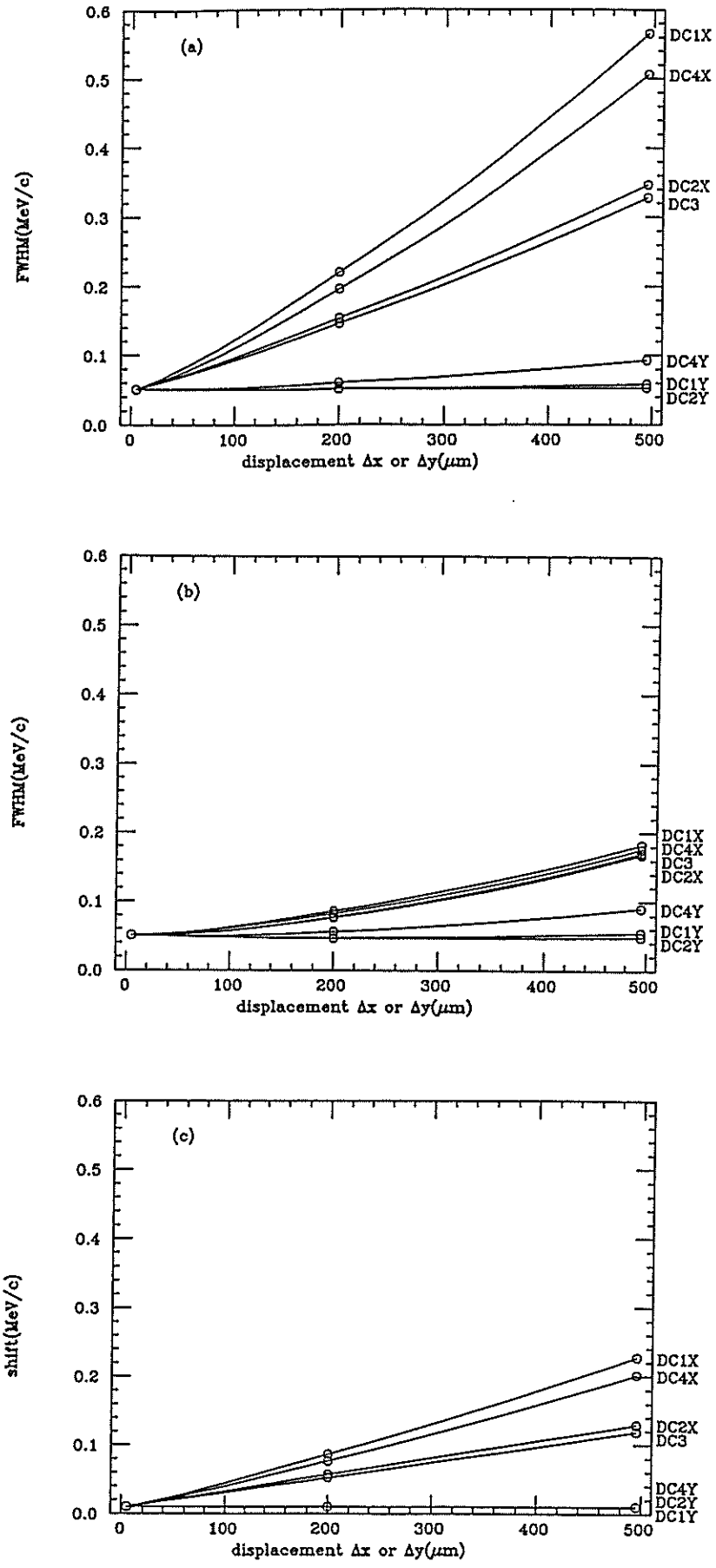

Figure 3.3: Momentum resolution as a function of the displacement of each drift chamber. (a) is for the momentum resolution around $\Delta p = 0$, (b) around the center of Δp distribution and (c) for the momentum shift from $\Delta p = 0$.

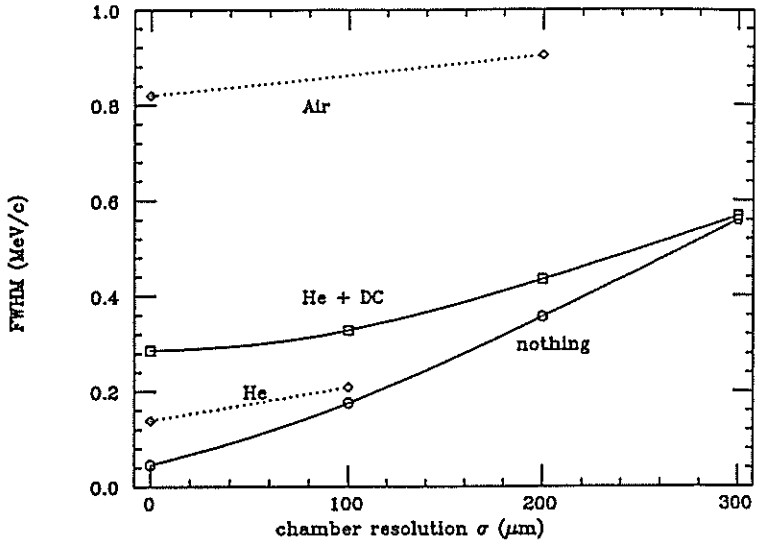

Figure 3.4: Momentum resolution v.s the drift chamber resolution with multiple scattering. Here the σ has the same meaning as fig. 3.1.

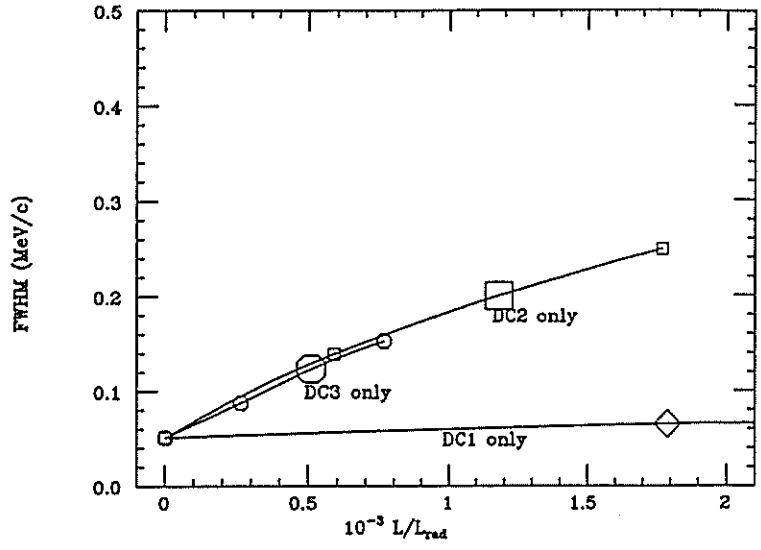

Figure 3.5: Momentum resolution as a function of L/L_{rad}. Each curve is calculated including multiple scattering of only one drift chamber. The large symbol stands for our case of L/L_{rad}.

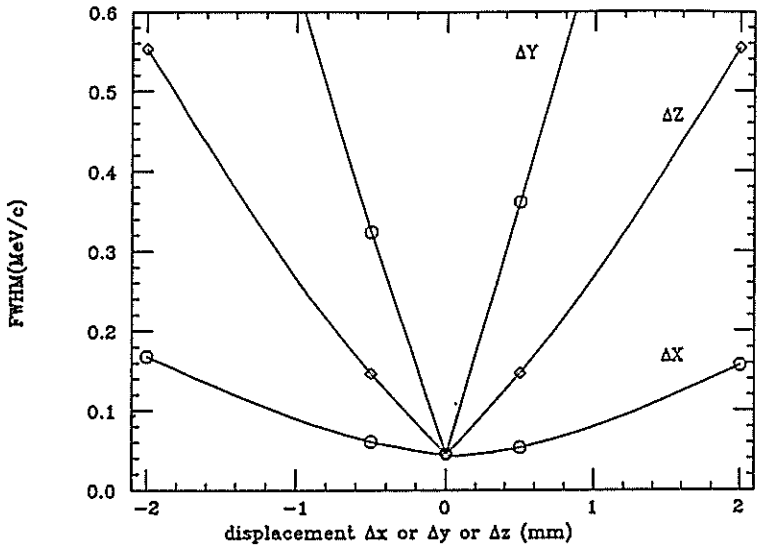

Figure 3.6: Momentum resolution as a function of the displacement of the magnetic field map.

Parallel displacement

In fig. 3.6 is shown the momentum resolution under the condition that there is intentional parallel displacement of the magnetic field map in the three kinds of direction. From fig. 3.6, we can find that the displacement in the Y direction has larger effect than in the Z direction whereas in the X direction little effect. The large effect from the Y direction is understandable in the respect that only the displacement in the Y direction can change largely the $\int \vec{B} \cdot \vec{dr}$ that is responsible for the momentum measurement.

Assuming the ΔX, ΔY and ΔZ can be smaller than $500\mu m$, the momentum resolution should be better than $\sqrt{0.35^2 + 0.15^2 + 0.5^2} \approx 0.62 MeV/c$ (FWHM).

Overall inclination

In fig. 3.7 is shown the momentum resolution under the condition that there is intentional overall inclination of the magnetic field map. This inclination corresponds to the distortion or the inclination of the whole structure of the instrument for magnetic field measurement. From fig. 3.7, we can find that all the three kinds of inclination have similar influence on the momentum resolution. Assuming that the accuracy is better than 0.5mrad, we can conclude that these errors can be ignored compared to the other factors.

Tilt of $\vec{B}$

Figure 3.8 shows the momentum resolution under the condition that there is intentional tilt of $\vec{B}$ at each point. This tilt would arise from the installation inaccuracy of the three Hall probes. It should be noted that this tilt is different from the overall inclination of the magnetic field map. From fig. 3.8, we can

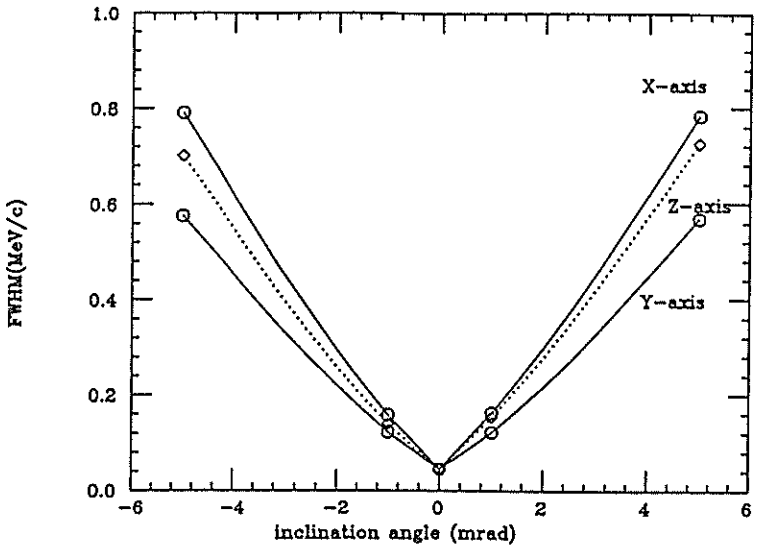

Figure 3.7: Momentum resolution as a function of the overall inclination angle of the magnetic field map about X-axis, Y-axis and Z-axis.

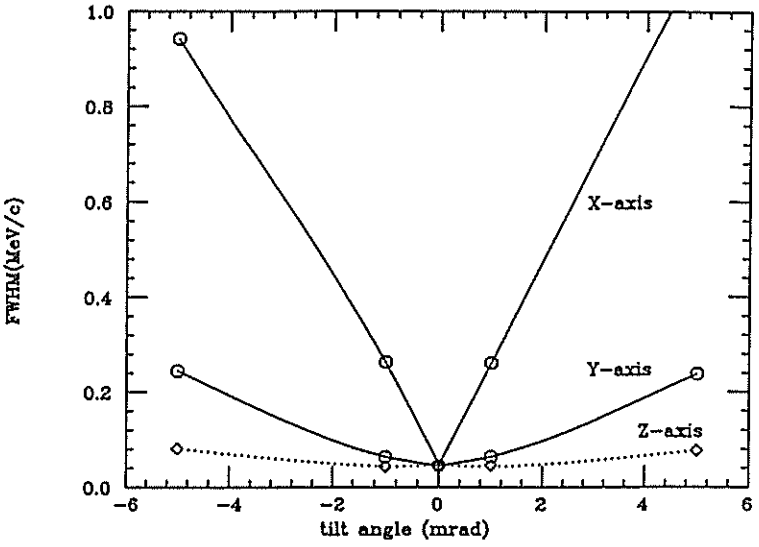

Figure 3.8: Momentum resolution as a function of the tilt angle of $\vec{B}$ at its own point.

find that the tilt about the X-axis considerably affects the momentum resolution whereas those about the Y-axis and Z-axis affect little. The little influence about the Z-axis is reasonable because the tilt does not change the main component of the magnetic field B_z. Granted that accuracy of the direction of the Hall probes is better than 1 mrad [53], the momentum resolution should be better than $\sqrt{0.25^2 + 0.05^2 + 0.05^2} \simeq 0.26 MeV/c$ (FWHM).

Others

We expect the calibration accuracy of the Hall probes to be better than 0.01% including the Hall planer effect and temperature dependence. This accuracy would correspond to the momentum resolution of $\sim 0.1 MeV/c$ (FWHM).

The stability of the current supply is also expected to be better than 0.01%

item	momentum resolution (FWHM)	presumed conditions
drift chamber resolution	0.35MeV/c	$\sigma \leq 200\mu m$
multiple scattering	0.2MeV/c	refer to Table 3.1
drift chamber position errors	0.35MeV/c	$\leq 200\mu m$
inaccuracy of magnetic field map	0.69MeV/c	position accuracy $\leq$ 0.5mm direction accuracy $\leq$ 1mrad Hall probe calibration $\leq$ 0.01%
total	0.87MeV/c	

Table 3.2: Momentum resolution of the SKS for $620 \sim 820 MeV/c$.

both in short term and long term.

summary

Overall momentum resolution amounts to $\sqrt{0.62^2 + 0.26^2 + 0.1^2 + 0.1^2} \approx 0.69 MeV/c$ (FWHM).

3.2.5 Summary

We have evaluated all the factors that affect the momentum resolution of the SKS, which are summarized in Table 3.2. Overall momentum resolution amounts to $\sqrt{0.35^2 + 0.2^2 + 0.35^2 + 0.69^2} \approx 0.87 MeV/c$ (FWHM). The multiple scattering has smaller influence on the momentum resolution compared with the others. The most important is accuracy of the magnetic field map.

Therefore we examine the dependence of the momentum resolution on the accuracy of the field map. Table 3.3 shows the resolution for three cases of the accuracy. The *case*0 represents the most probable case. The momentum resolution is sensitive to the variation. Thus, the magnetic field measurement is very important to achieve the good momentum resolution of the SKS. We can conclude that the good momentum resolution about 0.1% would be possible.

case	accuracy of the magnetic field map			total momentum resolution (FWHM)
	position	direction	calibration	
*case*0	0.5mm	1mrad	0.01%	0.87MeV/c
*case*1	0.2mm	0.5mrad	0.01%	0.63MeV/c
*case*2	1mm	2mrad	0.02%	1.11MeV/c

Table 3.3: Expected momentum resolution of the SKS with the three kinds of accuracy for the magnetic field map.

3.3 Energy resolution

In this section, we estimate the energy resolution for the Λ-hypernuclear experiments by the (π^+, K^+) reaction. In this case, the momentum of the pion set to be about $1050 MeV/c$ and that of the kaon is around $720 MeV/c$. As mentioned at the beginning of this chapter, mainly three points limit the energy resolution; the momentum resolution of the SKS, the momentum resolution of the beam line spectrometer, and the energy loss fluctuation in the target.

3.3.1 Effect of momentum resolution on the energy resolution

The momentum resolution of the SKS

The hypernuclear mass is calculated with the energy conservation law as follows,

$$M_{hy} = \sqrt{(E_\pi + M_A - E_K)^2 - (p_\pi^2 + p_K^2 - 2p_\pi p_K \cos\theta)}, \tag{3.3}$$

where M_A and M_{hy} are mass of the target nucleus and of the produced hyper nucleus; $E_{\pi,K}$ and $p_{\pi,K}$ are the energy and the momentum of the incident π mesons and outgoing K mesons, respectively; θ is the reaction angle. Using this relation, the energy resolution, ΔM_{hy}^{SKS} (FWHM), can be estimated with (refer to Appendix H)

$$\begin{aligned} \Delta M_{hy}^{SKS} &= \left(\frac{\partial M_{hy}}{\partial p_K}\right) \Delta p_{SKS} \\ &\simeq \left(\frac{p_K}{E_K}\right) \Delta p_{SKS} \simeq 0.83 \Delta p_{SKS}, \end{aligned} \tag{3.4}$$

where Δp_{SKS} (FWHM) is the momentum resolution for the outgoing kaon and here $p_K \simeq 720 MeV/c$ is used.

The momentum resolution of the beam line spectrometer.

Similarly, we can calculate the energy resolution, ΔM_{hy}^{beam} (FWHM), as follows;

$$\Delta M_{hy}^{beam} \simeq \left(\frac{p_\pi}{E_\pi}\right) \Delta p_{beam} \simeq 0.98 \Delta p_{beam}, \tag{3.5}$$

where Δp_{beam} (FWHM) is the momentum resolution for the incoming pion and here $p_\pi \simeq 1050 MeV/c$ is used.

Since we expect the momentum resolution to be better than $1 MeV/c$(FWHM) (see section 1.5), we can get,

$$\Delta M_{hy}^{beam} \simeq 0.98 \times 1 MeV/c \simeq 1 MeV. \tag{3.6}$$

3.3.2 Energy loss fluctuation in the target

We use the Landau's approximation for estimation of the energy loss fluctuation by the target here. This approximation is valid only when the mean energy loss is large compared to the binding energy of the most tightly bound electron, but small compared to the maximum possible energy loss in a single collision (see Appendix H). For a experimental target to be used, however, the latter condition is not true. As a result, we would overestimate it, but only slightly [54].

In the Landau's approximation, energy loss fluctuation, ΔE, (FWHM) can be calculated with the following relation (see Appendix H).

$$\Delta E = 0.617 \left(\frac{Z_{med}(\rho_{med} t_{med})}{A_{med}}\right) \left(\frac{Z_{inc}}{\beta}\right)^2, \tag{3.7}$$

Z_{med} and A_{med} are the atomic number and the mass number of the medium; ρ_{med} and t_{med} are the mass density in g/cm^2 and the thickness in cm of the medium; Z_{inc} and β are the charge number and the velocity of the projectile.

In addition, we could not know the reaction point in the target. This ambiguity causes another uncertainty of energy loss because of the difference of the mean energy loss between pion and kaon. In total, we can get the following relation for the energy resolution ΔM_{hy}^{target} (see appendix H);

$$\Delta M_{hy}^{target} = \sqrt{\frac{1}{3}(\Delta E_K^2 + \Delta E_\pi^2) + \frac{2.35^2}{3}\left\{\left(\frac{dE}{dx}\right)_K t_{med} - \left(\frac{dE}{dx}\right)_\pi t_{med}\right\}^2}, \tag{3.8}$$

in the unit of FWHM, where $\Delta E_{K,\pi}$ is to be calculated with the Landau's approximation and $(\frac{dE}{dx})_{K,\pi} t_{med}$ should be calculated with the Bethe-Bloch formula.

Table 3.4 shows the mean energy loss in various targets per 1g/cm^2, and the energy loss fluctuation per 1g/cm^2.

	^{12}C	^{28}Si	^{56}Fe	^{139}La	^{208}Pb
ΔE_K	0.45	0.45	0.41	0.37	0.35
ΔE_π	0.45	0.32	0.30	0.26	0.25
$\left(\frac{dE}{dx}\right)_K$	1.96	1.98	1.73	1.40	1.28
$\left(\frac{dE}{dx}\right)_\pi$	2.16	1.83	1.63	1.35	1.25
ΔM_{hy}^{target}	0.46	0.39	0.32	0.27	0.25

Table 3.4: The influence of the energy loss fluctuation on the energy resolution per g/cm^2. (unit: in MeV)

energy resolution (FWHM)	^{12}C	^{28}Si	^{56}Fe	^{139}La	^{208}Pb
2.5MeV	4.8	5.6	6.9	8.2	8.8
2.0MeV	3.5	4.1	5.0	5.9	6.4
1.5MeV	2.0	2.3	2.8	3.3	3.6

Table 3.5: The allowed target thickness to keep given energy resolution. (unit: in g/cm^2)

3.3.3 Overall energy resolution

We have evaluated the three factors which determine the energy resolution. The influence of the momentum resolution of the two spectrometers amount to the energy resolution of $\sqrt{0.83^2 0.87^2 + 1.0^2} \simeq 1.2 MeV$(FWHM) assuming the $case0$ in Table 3.3. The target thickness should be selected for a compromise between good energy resolution and good statistics. Table 3.5 shows the allowed thickness for various targets to keep given energy resolution. We can find the energy resolution better than $2MeV$ would be possible with a realistic target thickness.

Chapter 4

Summary

In chapter 1, we showed that the SKS was very useful for the hypernuclear spectroscopy by the (π, K) reaction, where the good energy resolution and the large acceptance were very crucial. We explained the design principle and the expected performance of the SKS and mentioned that the SKS would play an indispensable role for the nuclear physics experiments around $1GeV/c$. In the last part, we described the detector system of the SKS.

In chapter 2, we described the silica aerogel Cerenkov counters in detail. The silica aerogel Cerenkov counters play an important role to veto pions in order to trigger kaons. We tested the prototype counter with the $0.7GeV/c$ pion beam and got enough efficiency with it. The Monte Carlo simulation well accounted for the results of the test experiment. Based on the conclusions of the test experiment and the considerations with the Monte Carlo simulation, we have designed a counter whose size is about 1.2m $\times$ 1.4m with the thickness of 40cm. We showed the efficiency better than 96.5% could be obtained for $0.7GeV/c$ pions. Since we decided to adopt the two layer system, accordingly, we could expect the efficiency better than 99.9% with the two counter.

In chapter 3, we studied the momentum resolution of the SKS. The good momentum resolution is one of the most important performance of the SKS. We evaluated all the factors which could affect the resolution with the Monte Carlo simulation. We showed that accuracy of the magnetic field map was the most crucial in order to achieve the momentum resolution as good as about 0.1%. In the latter half, we estimated the energy resolution for the Λ-hypernuclear mass taking into account the momentum resolution of the SKS and the beam line spectrometer, and the energy loss fluctuation in the target. We showed that the resolution better than $2MeV$ could be achieved with a realistic target thickness.

Appendix A

Experimental yields estimation

First, we estimate expected experimental yields for Λ-hypernuclei production by the (π^+, K^+) reaction with various targets, ^{12}C, ^{28}Si, ^{56}Fe, ^{139}La and ^{208}Pb.

Experimental yields, Y_{hyper}, are calculated with the following relation

$$Y_{hyper} = I_{\pi+}\,\Omega\,F_{ang}\,S_{K+}\,\varepsilon_{ana}\,\left.\frac{d\sigma}{d\Omega}\right|_{\theta=0} T_{thick}, \tag{A.1}$$

where the symbols are defined in Table A.1, Table A.2 and Table A.3. The angular reduction factor, F_{ang}, stands for the fact that the cross section decreases with the reaction angle θ increasing. This value, $F_{ang} = 0.6$, is estimated using theoretical calculations for ^{12}C [20] and ^{28}Si [55]. The analysis efficiency, ε_{ana}, represents the drift chamber efficiency, the momentum reconstruction efficiency and so on. The T_{thick} is the number of nuclei in a unit area of the target. They are so chosen that the mass resolution is better than $2MeV$(FWHM) (see section 3.3.3). Calculated differential cross section with DWIA is shown in Table A.3.

Table A.4 shows estimated experimental yields for various Λ-hypernuclear states.

Similarly, we estimate expected experimental yields for the reaction $^{28}Si(\pi^-, K^+)^{28}_{\Sigma}Mg$ (Table A.5). Though, the yields are much smaller than those for the Λ-hypernuclei, they are still in our practical reach. Thus, the large acceptance of 100msr is very

item	symbol	
π^+ intensity	$I_{\pi+}$	1.7×10^{11}particles/day $(2 \times 10^6$particles/sec)
acceptance	Ω	$0.1sr$
angular reduction	F_{ang}	0.6
K^+ survival rate	S_{K+}	0.35
analysis efficiency	ε_{ana}	0.5

Table A.1: The parameters used for the yields estimation.

hyper-nucleus	thickness	
	g/cm^2	numbers of nuclei/cm^2
${}^{12}_{\Lambda}C$	3.5	1.8×10^{23}
${}^{28}_{\Lambda}Si$	4.1	8.8×10^{22}
${}^{56}_{\Lambda}Fe$	5.0	5.4×10^{22}
${}^{139}_{\Lambda}La$	5.9	2.6×10^{22}
${}^{208}_{\Lambda}Pb$	6.4	1.9×10^{22}

Table A.2: The target thickness, T_{thick}, used in the yields estimation.

hyper-nucleus	n state	Λ orbit					
		0s	0p	0d	0f	0g	0h
${}^{12}_{\Lambda}C$	$0p^{-1}_{3/2}$	17.	24.	-	-	-	-
${}^{28}_{\Lambda}Si$	$0d^{-1}_{5/2}$	8.8	24.	26.	-	-	-
${}^{56}_{\Lambda}Fe$	$0f^{-1}_{7/2}$	3.8	14.	25.	-	-	-
${}^{139}_{\Lambda}La$	$0h^{-1}_{11/2}$	-	4.3	9.9	20.	20.	-
${}^{208}_{\Lambda}Pb$	$0i^{-1}_{13/2}$	-	3.0	6.7	11.	17.	17.

Table A.3: Calculated differential cross section, $\frac{d\sigma}{d\Omega}\Big|_{\theta=0}$, for various hypernuclear states in the unit of $\mu b/sr$ (with DWIA by T.Motoba et al.[20]).

hyper-nucleus	n state	Λ orbit					
		0s	0p	0d	0f	0g	0h
${}^{12}_{\Lambda}C$	$0p^{-1}_{3/2}$	5.5	7.7	-	-	-	-
${}^{28}_{\Lambda}Si$	$0d^{-1}_{5/2}$	1.4	3.8	4.1	-	-	-
${}^{56}_{\Lambda}Fe$	$0f^{-1}_{7/2}$	.37	1.3	2.4	-	-	-
${}^{139}_{\Lambda}La$	$0h^{-1}_{11/2}$	-	.15	.46	.93	.93	-
${}^{208}_{\Lambda}Pb$	$0i^{-1}_{13/2}$	-	.10	.23	.37	.58	.58

Table A.4: Expected experimental yields for various hypernuclear states ($\times 10^3/day$).

states			$\frac{d\sigma}{d\Omega}\Big\|_\theta = 0$	/day	/1-month
n	Σ^-	j^π			
$d_{5/2}^{-1}$	$s_{1/2}$	2^+	$0.20\mu b/sr$	31	930
$d_{5/2}^{-1}$	$p_{3/2}$	3^-	$0.27\mu b/sr$	42	1260
$d_{5/2}^{-1}$	$p_{1/2}$	3^-	$0.14\mu b/sr$	22	660

Table A.5: Calculated cross section for $^{28}Si(\pi^-, K^+)^{28}_{\Sigma}Mg$ at $p_\pi = 1.25MeV/c$, with DWIA by T.Motoba et al.[33], and expected experimental yields.

important for small cross section experiments.

Appendix B

Modification of the PMT's

Our PMT's (R1584-SKS) are modified from the original design, HAMAMATSU R1584-01, as follows.

First, the resistance distribution of divider circuit is changed as shown in fig. B.1 to improve the one-photoelectron resolution. Figure B.2 shows a comparison of the resolution between R1584-SKS and original R1584-01 and RCA8854. We can find that R1584-SKS is better than R1584-01 whereas it is comparable to RCA8854 in the resolution. Second, in order to reduce the dark current, the photoelectric cathodes are connected with the ground (see B.2), hence the supplied voltage is positive.

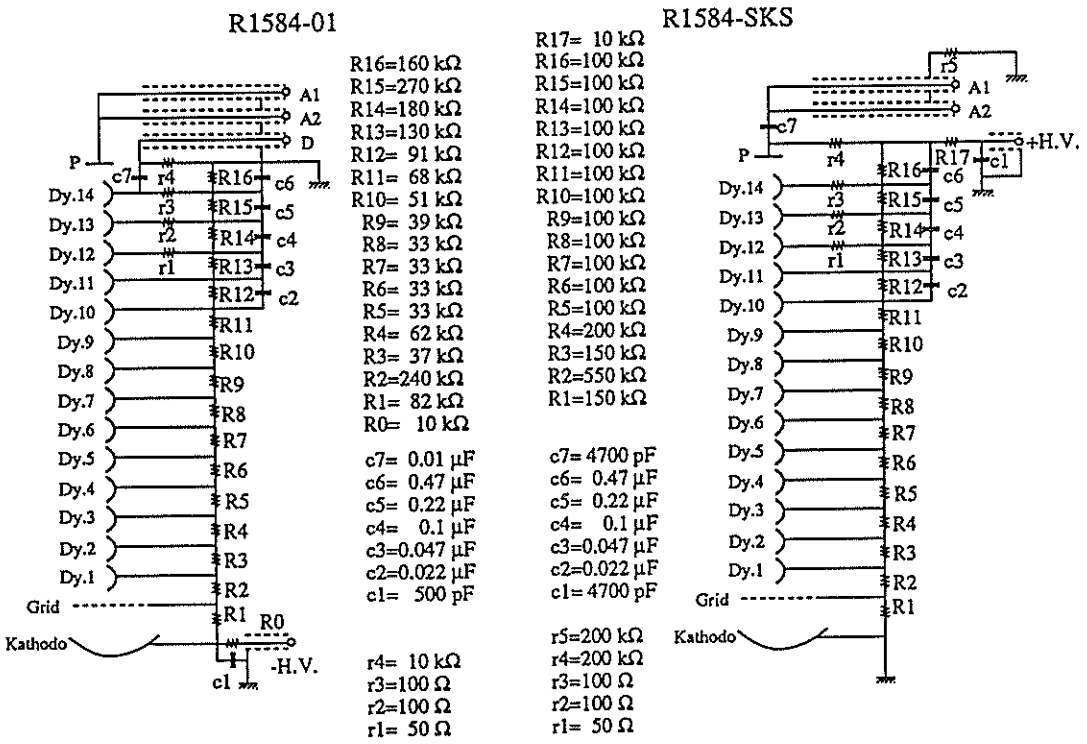

Figure B.1: The divider circuits of R1584-01 and R1584-SKS.

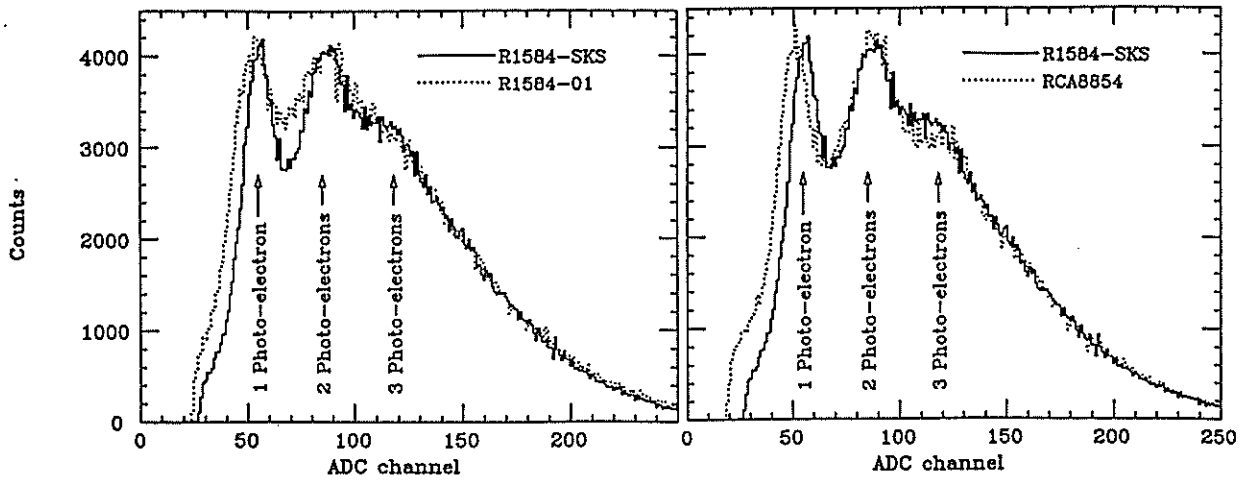

Figure B.2: Comparison of the one-photoelectron resolution between R1584-SKS, R1584-01 and RCA8854.

Appendix C

Calculation of the mean photoelectron number $\overline{N_e}$

The mean photoelectron number, $\overline{N_e}$, is calculated by fitting the following function to the sum ADC spectrum of the six PMT's;

$$C_{norm.} \sum_{n_{p.e.}=1}^{max} \frac{e^{-\lambda}}{n_{p.e.}!} \lambda^{n_{p.e.}} \frac{1}{\sqrt{2\pi\bar{\sigma}^2 n_{p.e.}}} exp\left(-\frac{(x - n_{p.e.}\bar{\mu})^2}{2n_{p.e.}\bar{\sigma}^2}\right), \qquad \text{(C.1)}$$

with $\lambda \equiv \overline{N_e}$, where $C_{norm.}$ is a normalization factor; $\bar{\sigma}$ and $\bar{\mu}$ are the mean values of the one-photoelectron resolution and the one-photoelectron peak position respectively, for the six PMT's in the unit of ADC channel. This function is essentially a superposition of Gaussian with the Poisson distribution being the weight. Here λ and $C_{norm.}$ are the parameters to be optimized in the fitting process. The resolution σ and the one-photoelectron peak position μ for each PMT are calculated by the similar fitting process to a ADC spectrum of one PMT. In this case, four parameters $C_{norm.}$, λ, σ and μ are the parameters to be optimized.

Figure C.1 shows typical ADC spectra and fitted curves with the optimized parameters. Note that the high voltage for the PMT's was so adjusted that the one-photoelectron peak positions for the six PMT's were equal.

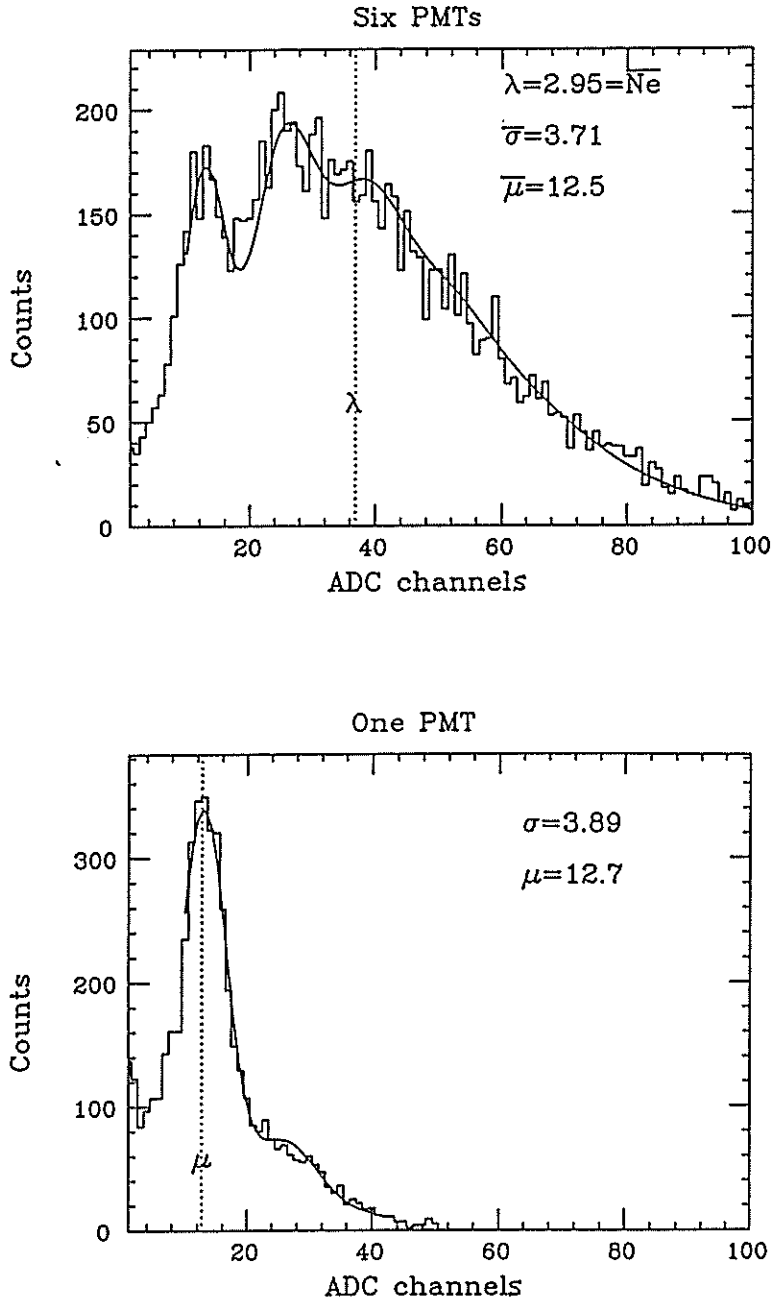

Figure C.1: Typical ADC spectra and fitted curves with the optimized parameters.

Appendix D

Magnetic shield test

The fringing magnetic field from the SKS will be about 300gauss around the silica aerogel cerenkov counters when the SKS is fully excited (see fig. 1.6). Hence, the PMT's need powerful magnetic shields.

We tested four kinds of magnetic shields (see Table D.1). They are all iron cylinders not rebaked. We employed a NaI light pulser with ^{207}Bi as the standard light source, and the TOKIWA magnet in KEK as the magnetic field source, which could produce over 300gauss in a sufficiently large volume. We measured the pulse height with a oscilloscope. We used R1584-SKS and set the supplied voltage to be +2.3kV.

The magnetic field was set to be 100, 200 and 300gauss in their magnitude, $\theta = 90°, 60°, 30°$ in their directions, where the θ is defined in fig. D.1. In these environments, we measured the pulse height with changing the parameter a or b. Here a and b are defined in fig. D.1. The results are summarized in fig. D.2 and D.3 for the parameter a, and in Table D.2 for the parameter b.

The angle θ should be larger than 60°. Otherwise, in order to keep the original pulse height, we must employ the heavier magnetic shield, but it is very hard to handle such heavy iron cylinders. Since the direction of the SKS fringing field is about 20° from the vertical direction around the silica aerogel Cerenkov counters, we decided to install the PMT's horizontally on the counter boxes. The ♯4 is better

name	thickness(diameter,length)
♯1	μ-metal + 2mm(16.5cm,50cm)
♯2	μ-metal + 5mm(16.5cm,50cm)
♯3	μ-metal + 2mm(16.5cm,50cm) + 5mm(19cm,50cm)
♯4	μ-metal + 5mm(16.5cm,50cm) + 5mm(19cm,50cm)
μ-metal	1mm(15cm,15cm)

Table D.1: The four kinds of iron cylinders tested.

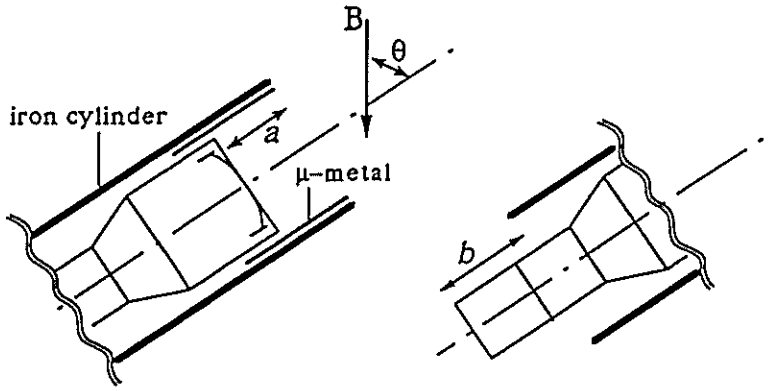

Figure D.1: The definition of the parameters a and b.

one, and the parameter a should be larger than $12cm \sim 15cm$ and the parameter b should be smaller than $7cm \sim 10cm$.

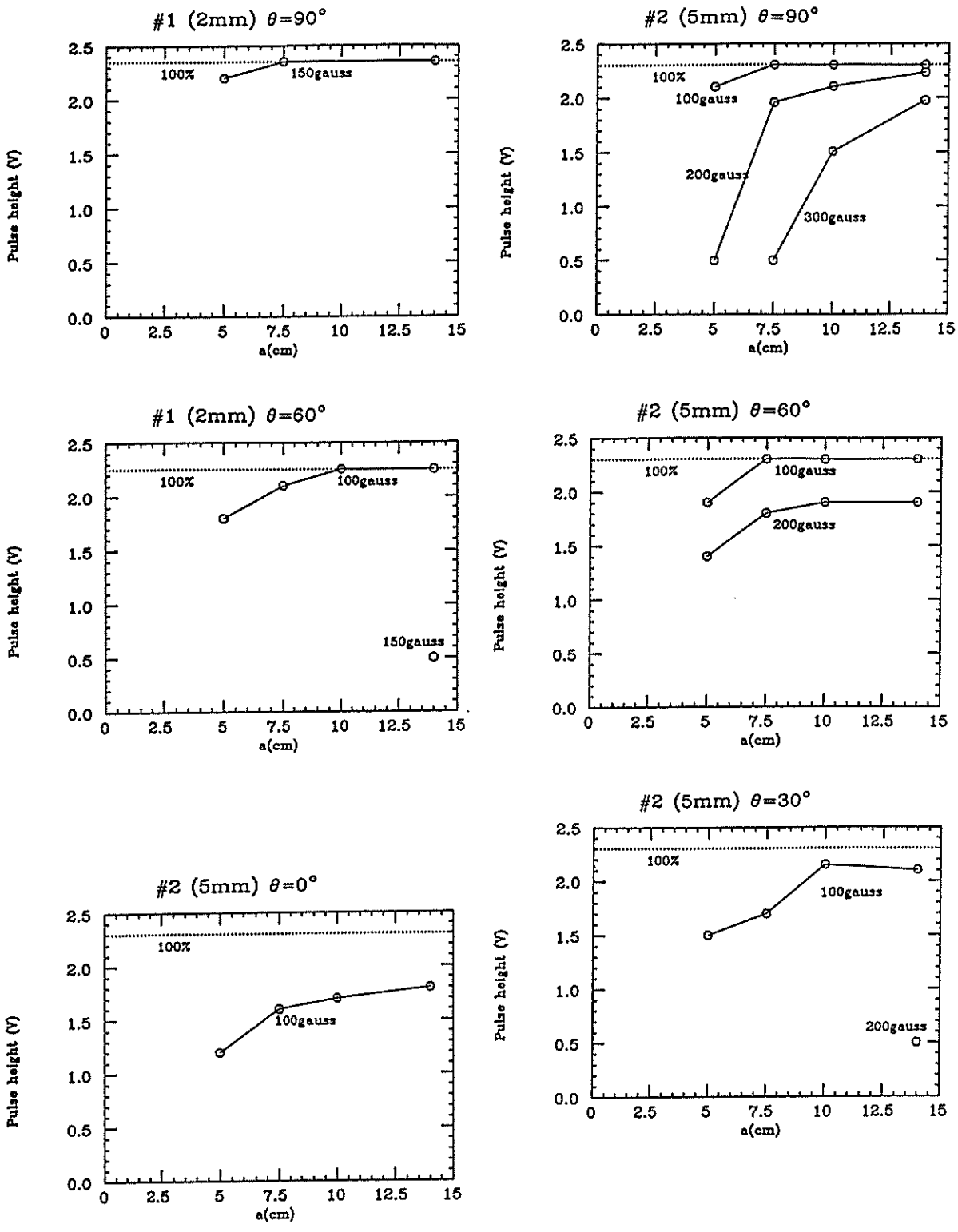

Figure D.2: Results of the magnetic shield test for the parameter a. The symbols ♯1 and ♯2 are defined in Table D.1.

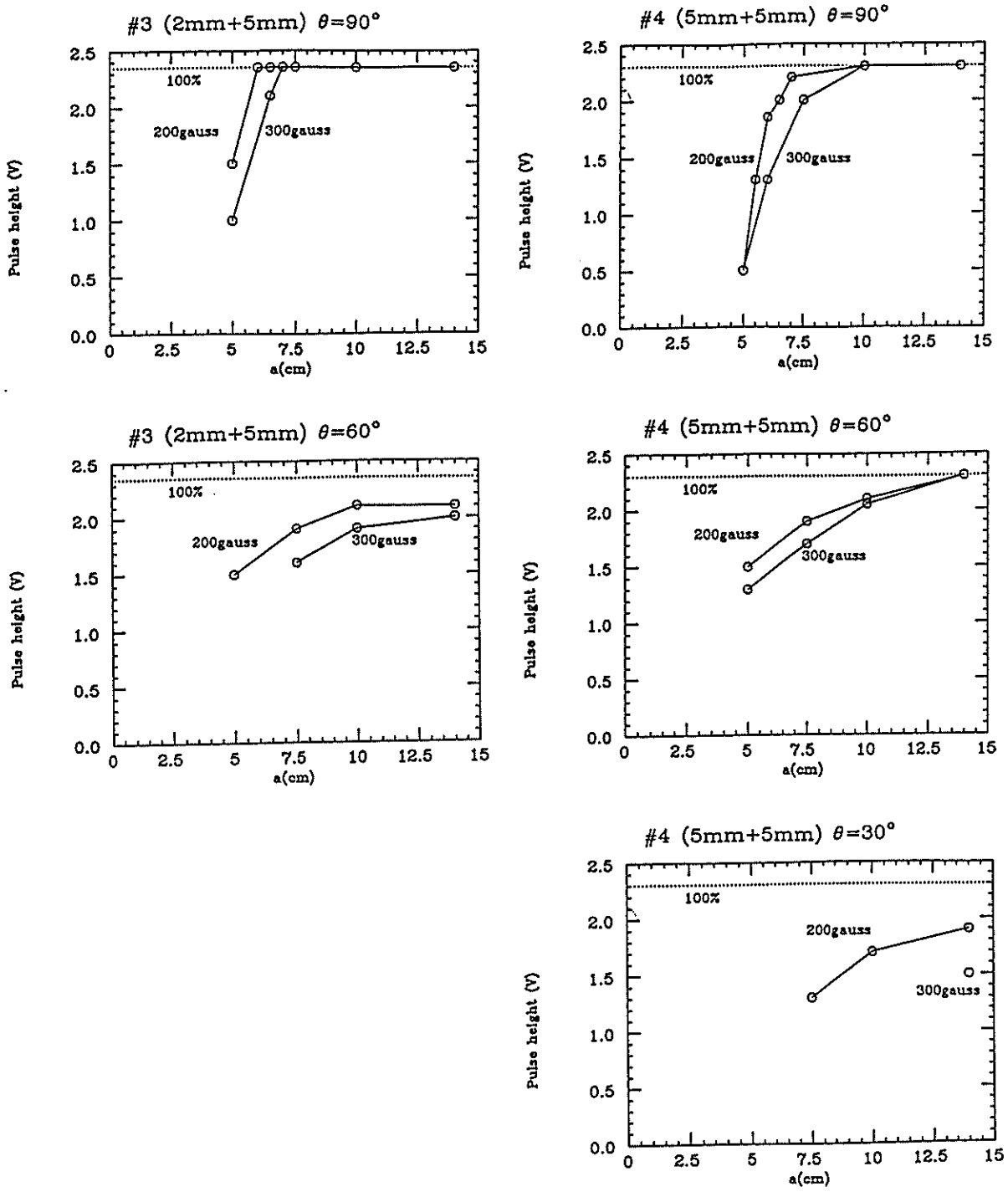

Figure D.3: Results of the magnetic shield test for the parameter a. The symbols ♯3 and ♯4 are defined in Table D.2.

shield	θ	$\lvert\vec{B}\rvert$	$b_{P.H.100\%}$
♯1	90°	150gauss	20cm
	60°	100gauss	10cm
♯3	90°	200gauss	19cm
		300gauss	18cm
	60°	300gauss	5 $\sim$ 10cm
♯4	90°	200gauss	20cm
		300gauss	18cm
	75°	200gauss	7 $\sim$ 10cm
		300gauss	7 $\sim$ 10cm
	60°	200gauss	10 $\sim$ 12cm
		300gauss	11cm

Table D.2: Results of the magnetic shield test for the parameter b. Here, the $b_{P.H.100\%}$ is the largest value of b where the pulse height is kept to be 100%.

Appendix E

Humidity dependence of the silica aerogel

Silica aerogel is generally very weak to moisture because moisture makes the transparency much worse. Hence we must keep it dry. We investigated the weakness of our silica aerogel to moisture, to some extent, quantitatively.

We employed the transmissivity as a measure of the deterioration of the transparency of the silica aerogel. The transmissivity is a mixture of two properties, those are, the attenuation length and the scattering length. If one uses relatively thin samples compared to the scattering length, the following relation is a good approximation,

$$\frac{1}{L_{trans}} = \frac{1}{L_{scat}} + \frac{1}{L_{att}} \sim \frac{1}{L_{scat}}, \tag{E.1}$$

where L_{trans}, L_{scat} and L_{att} are the transmission length, the scattering length and the attenuation length respectively. Here, the latter "$\sim$" is valid because L_{scat} is much smaller than L_{att} in general. Therefore, the transmissivity is mainly related to the scattering length.

We used a spectro photometer to measure the transmissivity. The size of the samples was about 10cm $\times$ 5cm $\times$ 3cm. The lights of the spectro photometer penetrated a sample in the 3cm direction. First, we measured their transmissivity. The measurement was done for three certain points for each sample and we took the mean value of the three. Second, we exposed those samples in five kinds of environment, where humidity is $\sim$ 20%, $\sim$ 35%, $\sim$ 40%, $\sim$ 50% and over 60% and at temperature of $23°C$ in all cases. After one week and after two weeks, We measured their transmissivity again. Results are summarized in Table E.1. We can conclude that 20 $\sim$ 35% is the threshold to keep their good transparency.

We also investigated the influence of N_2 gas on the transparency of the silica aerogel. The measurement was done in a similar way. The result was that this environment was very good one that was comparable to the case of 20%.

Note that the results are limited to the short term variation of the properties

duration	humidity					
	$\sim 20\%$	$\sim 20\%$	$\sim 35\%$	$\sim 40\%$	$\sim 50\%$	$\geq 60\%$
initial value	10.3	11.3	10.6	10.7	11.3	11.4
after 1 week	+1.3	+1.3	+0.6	+0.6	-1.3	-0.4
after 2 weeks	+1.1	+1.3	-0.4	-0.4	-1.2	-1.8

Table E.1: The humidity dependence of the transmissivity (%) of our silica aerogel (at 400nm and $23°C$). The precision of transmissivity is better than 0.2%.

of a few pieces of the silica aerogel and to the wave length of 400nm.

Appendix F

Multiple scattering

In general, distribution of deflection angle by multiple scattering is subjected to the gaussian distribution as follows,

$$distribution = \frac{1}{2\pi\theta_0^2} exp\left(-\frac{\theta^2}{2\theta_0^2}\right) d\Omega, \tag{F.1}$$

with

$$\theta_0 = \frac{14.1}{p\beta} Z\sqrt{\frac{L}{L_{rad}}}\left(1 + \frac{1}{9} log_{10}(\frac{L}{L_{rad}})\right), \tag{F.2}$$

where p, β and Z are the momentum (in MeV/c), velocity and charge number of the incident particle; L/L_{rad} is the thickness of the scattering medium in radiation length. The L_{rad} is defined as the distance over which a high energy electron (≥ 1 GeV for most materials) loses all but a fraction $1/e$ of its energy to Bremsstrahlung, on average. It should be noted that the multiple scattering has no connection with Bremsstrahlung. Here L/L_{rad} appears as the parameter that characterizes the scattering medium. Therefore it is useful to measure the thickness in terms of radiation length.

Appendix G

Additional studies for the momentum resolution of the SKS

First, we examine how much each drift chamber information contributes to the momentum resolution of the SKS using the Monte Carlo simulation. Figure G.1 shows the momentum resolution when one of the seven kinds of position information (see section 3.2.1) is not used for the momentum reconstruction. They include the effects of the multiple scattering and the drift chamber resolution ($\sigma = 200\mu m$). We can find that DC1 and DC4 are much contributory than DC2 and DC3. The DC4Y is important whereas DC1Y has less contribution.

Second, we examine how much the momentum resolution changes when the position of DC4 or the target is displaced along the central track. Here, the displacement of DC4 is limited to the forward direction and that of the target to the backward direction. The results are shown in fig. G.2. There are little changes in the momentum resolution in both cases.

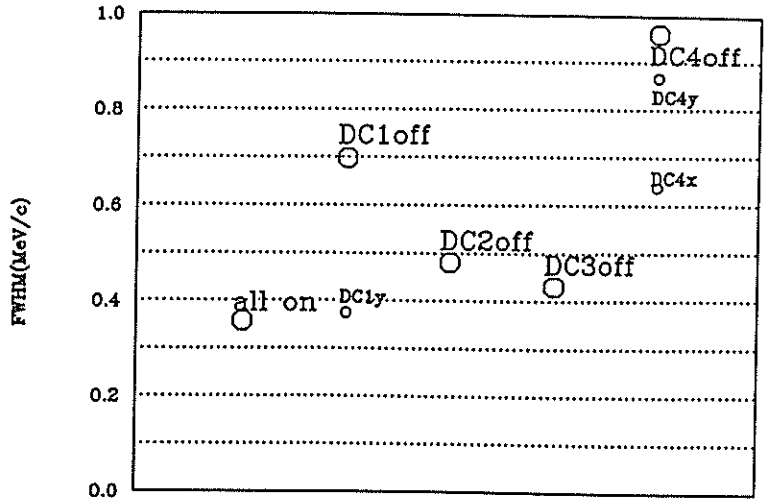

Figure G.1: Momentum resolution of the SKS when one of the seven kinds of position information is not used for the momentum reconstruction, including the effects of the multiple scattering and the drift chamber resolution ($\sigma = 200\mu m$) .

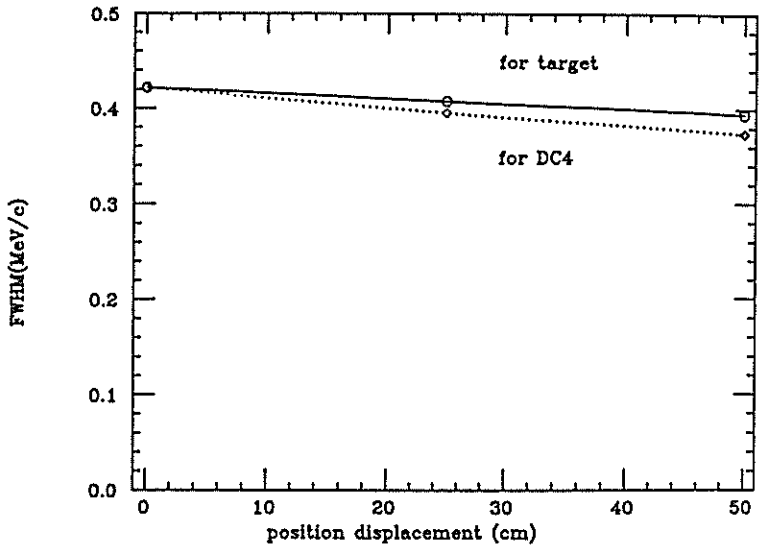

Figure G.2: Momentum resolution of the SKS when the position of DC4 or of the target is displaced along the central track, including the effects of the multiple scattering and the drift chamber resolution ($\sigma = 200\mu m$). The displacement is to the forward for DC4, and to the backward for the target.

Appendix H

The Landau's approximation for energy loss fluctuation

The mean energy loss of a heavy projectile (much massive than a electron) in a medium can be calculated by the Bethe-Bloch equation. Around the mean value, the actual energy loss varies due to the statistical nature of the phenomenon. If the mean energy loss is large compared to the binding energy of the most tightly bound electron but small compared to the maximum possible energy loss in a single collision, the Landau approximation is available for estimation of the energy loss fluctuation [56,57,58]. Let $\chi(W,t)dW$ be the probability that the projectile loses an energy between W and $W+dW$ after crossing the thickness t of the medium, the Landau's approximation says

$$\chi(W,t) = \frac{1}{\xi}\frac{1}{\pi}\int_0^\infty exp\{-u\,(\ln u + \lambda)\}\sin \pi u\; du, \tag{H.1}$$

with

$$\lambda \equiv \frac{1}{\xi}\left\{W - \xi\left(\ln\frac{\xi}{\epsilon'} + 1 - C_E\right)\right\}, \tag{H.2}$$

$$\ln\epsilon' \equiv \ln\frac{(1-\beta^2)I^2}{2(m_e c^2)\beta^2} + \beta^2, \tag{H.3}$$

$$C_E \equiv 0.577\ (\text{Euler's constant}), \tag{H.4}$$

and

$$\xi \equiv \frac{1}{2}\left\{\frac{D\,Z_{med}\,\rho_{med}}{A_{med}}\left(\frac{Z_{inc}}{\beta}^2\right)\right\} t_{med}, \tag{H.5}$$

with $D \equiv 4\pi N_A r_e^2 m_e c^2 = 0.3070 MeV\,\text{cm}^2/\text{g}$, where Z_{med}, A_{med}, ρ_{med} and t_{med} are the charge number, the mass number, the mass density in g/cm^3 and the thickness in cm of the energy loss medium; I is the mean ionization energy of the medium; Z_{inc} and β are the charge number and the velocity of the projectile. A numerical calculation [56] gives the full width at half maximum of this distribution,

$$\text{FWHM} = 4.02\xi. \tag{H.6}$$

Appendix I

Effect of energy loss fluctuation on the energy resolution

Here we estimate analytically the influence of the energy loss fluctuation in the target on the energy resolution of the hypernuclear mass. Letting E_π and E_K be the energy of the pion and the kaon, respectively, we can estimate the deviation in the hypernuclear mass, M_{hy}, as follows,

$$\begin{aligned} dM_{hy} &= \frac{\partial M_{hy}}{\partial E_\pi} dE_\pi + \frac{\partial M_{hy}}{\partial E_K} dE_K \\ &= \frac{\partial M_{hy}}{\partial E_\pi} \left(\frac{dE}{dx}\right)_\pi t_{in} - \frac{\partial M_{hy}}{\partial E_K} \left(\frac{dE}{dx}\right)_K \frac{(t_{med} - t_{in})}{\cos\theta}, \end{aligned} \tag{I.1}$$

where t_{med} is the thickness of the target, and t_{in} is the distance between the reaction point and the incident surface (see fig. I.1), and θ is the reaction angle; $(\frac{dE}{dx})_{K,\pi}$ is not only the mean energy loss but including its fluctuation. Note the first negative sign in the second line. This is because the energy loss of the outgoing kaon make the momentum to be measured lower than the *true* momentum, that is, the momentum right after the reaction.

On the other hand, from the energy conservation law, we get

$$M_{hy} = \sqrt{(E_\pi + M_A - E_K)^2 - (p_\pi^2 + p_K^2 - 2p_\pi p_K \cos\theta)}, \tag{I.2}$$

where M_A is the target nuclear mass, hence we can find,

$$\begin{aligned} \frac{\partial M_{hy}}{\partial E_\pi} &= \frac{1}{M_{hy}} \left\{ M_A - E_K + \frac{p_K}{p_\pi} E_\pi \cos\theta \right\}, \\ \frac{\partial M_{hy}}{\partial E_K} &= \frac{1}{M_{hy}} \left\{ -M_A - E_\pi + \frac{p_\pi}{p_K} E_K \cos\theta \right\}. \end{aligned} \tag{I.3}$$

Here we adopt the following approximation,

$$\frac{\partial M_{hy}}{\partial E_K} \simeq -\frac{M_A}{M_{hy}} \simeq -1, \tag{I.4}$$

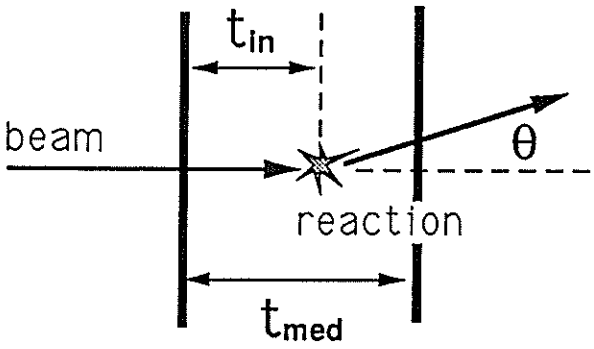

Figure I.1: The definition of t_{in} and t_{med}.

$$\cos\theta \simeq 1, \tag{I.5}$$

$$\left(\frac{\partial M_{hy}}{\partial E_\pi}\right) + \left(\frac{\partial M_{hy}}{\partial E_K}\right) = \frac{1}{M_{hy}}\left\{E_K\left(\frac{p_\pi}{p_K} - 1\right) - E_\pi\left(1 - \frac{p_K}{p_\pi}\right)\right\} \simeq 0, \tag{I.6}$$

which are well justified because now we are sufficient with the accuracy of about 10% for our purposes. Then we get

$$\begin{aligned} dM_{hy} &= \left\{\frac{\partial M_{hy}}{\partial E_\pi} + \frac{\partial M_{hy}}{\partial E_K}\right\}\left(\frac{dE}{dx}\right)_\pi t_{in} + \frac{\partial M_{hy}}{\partial E_K}\left\{\left(\frac{dE}{dx}\right)_K - \left(\frac{dE}{dx}\right)_\pi\right\} t_{in} \\ &\quad - \frac{\partial M_{hy}}{\partial E_K}\left(\frac{dE}{dx}\right)_K t_{med} \\ &= \left(\frac{dE}{dx}\right)_K t_{med} - \left\{\left(\frac{dE}{dx}\right)_K - \left(\frac{dE}{dx}\right)_\pi\right\} t_{in}. \end{aligned} \tag{I.7}$$

We can understand this relation intuitively by substituting 0 or t_{med} for t_{in}.

Though we can not estimate the fluctuation of the energy loss, we can correct the mean energy loss in the target. Accordingly, we define $dM_{hy,cor}$, which is the corrected dM_{hy}, as follows,

$$dM_{hy,cor} \equiv dM_{hy} - \left(\overline{\frac{dE}{dx}}\right)_K t_{med}, \tag{I.8}$$

here $(\frac{dE}{dx})_{K,\pi}$ is separated into two parts; one is the mean energy loss, $(\overline{\frac{dE}{dx}})_{K,\pi}$, and the other is its fluctuation $\delta_{K,\pi}$. Then we can write $dM_{hy,cor}$ as follows,

$$\begin{aligned} (dM_{hy,cor})^2 &= \left\{\left\{\left(\overline{\frac{dE}{dx}}\right)_K - \left(\overline{\frac{dE}{dx}}\right)_\pi\right\}^2 + \delta_K^2 + \delta_\pi^2\right\} t_{in}^2 \\ &\quad + \delta_K^2 t_{med}^2 - 2\delta_K^2 t_{in} t_{med} + O(\delta_K)O(\delta_\pi) + O(\delta_{K,\pi}). \end{aligned} \tag{I.9}$$

Taking the mean value using $\overline{t_{in}} = t_{med}/2$ and $\overline{t_{in}^2} = t_{med}^2/3$, and $\overline{O(\delta_{K,\pi})} = 0$, we get

$$\overline{(dM_{hy,cor})^2} = \frac{1}{3}\left\{\overline{(\delta_K t_{med})^2} + \overline{(\delta_\pi t_{med})^2}\right\} + \frac{1}{3}\left\{\left(\overline{\frac{dE}{dx}}\right)_K t_{med} - \left(\overline{\frac{dE}{dx}}\right)_\pi t_{med}\right\}^2, \tag{I.10}$$

or,

$$\Delta M_{hy} = \sqrt{\frac{1}{3}(\Delta E_K^2 + \Delta E_\pi^2) + \frac{2.35^2}{3}\left\{\left(\overline{\frac{dE}{dx}}\right)_K t_{med} - \left(\overline{\frac{dE}{dx}}\right)_\pi t_{med}\right\}^2}, \tag{I.11}$$

where ΔM_{hy}, ΔE_K^2 and ΔE_π^2 are in the unit of FWHM; $(\overline{\frac{dE}{dx}})_{K,\pi} t_{med}$ should be calculated with the Bethe-Bloch formula.

Acknowledgement

I would like to express my special thanks to Prof.O.Hashimoto for his continuous guidance and encouragement to my work, and for accepting me as a student in the graduate school. I also wish to thank Dr.T.Nagae and Ms.M.Sekimoto for their advice about experimental technique and computer systems. I am grateful to Dr.S.Toyama about the silica aerogel Cerenkov counters because my work is a continuation of his work. I also would like to thank Dr.H.Enyo for valuable discussion about the design of the silica aerogel Cerenkov counters. I express appreciation to Dr.Y.Kawashima for technical advice and crucial collaboration to the magnetic shield test. My vitality was very much stimulated by his high spirits. I also wish to thank Mr.K.Omata for his kind help about the data-taking program for personal computers. I wish to thank Mr.A.Higashi and Dr.I.Nomura for collaboration to the test experiment of the prototype silica aerogel Cerenkov counter. I am also grateful to the CP group in KEK for lending us the TOKIWA magnet for the magnetic shield test. Finally I would like to express my special thanks to Dr.Y.Akiba, Dr.T.Nagae and Prof.O.Hashimoto for their kind proof reading of my master thesis.

The SKS is under construction in KEK by Mr.K.Omata, Mr.T.Kitami, Ms.M.Sekimoto, Dr.T.Nagae, Prof.O.Hashimoto, Prof.S.Honma, Mr.Y.Matsuyama, Dr.T.Miyachi, Mr.T.Morimoto (INS), and Ms.K.Aoki, Mr.Y.Kondo, Prof.T.Shintomi, Prof.Y.Doi, Dr.Y.Makita (KEK).

Bibliography

[1] M.Danysz and J.Pniewski, Phil.Mag.**44**(1953)348.

[2] W.Brückner et al., Phys.Lett.**55B**(1975)107.

[3] G.C.Bonazzola et al., Phys.Rev.Lett.**34**(1975)683.

[4] W.Brückner et al., Phys.Lett.**62B**(1976)481.

[5] W.Brückner et al., Phys.Lett.**79B**(1978)157.

[6] R.Bertini et al., Phys.Lett.**83B**(1979)306.

[7] R.Bertini et al., Nucl.Phys.**A360**(1981)315.

[8] R.Bertini et al., Nucl.Phys.**A368**(1981)365.

[9] R.E.Chrien et al., Phys.Lett.**89B**(1979)31.

[10] M.May et al., Phys.Rev.Lett.**47**(1981)1106.

[11] E.H.Auerbach et al., Ann.Phys.**148**(1983)381.

[12] C.B.Dover et al., Phys.Rev.**C22**(1980)2073.

[13] H.Bando et al., Prog.Theor.Phys.**76**(1986)1321.

[14] C.Milner et al., Phys.Rev.Lett **54**(1985)1237.

[15] R.E.Chrien, Nucl.Phys.**A478**(1988)705c.

[16] M.Akei et al., Nuovo Cimento **102A**(1989)457.

[17] D.J.Millener et al., Phys.Rev.C **38**(1988)2700.

[18] M.Rufa et al., Phys.Rev.C **42**(1990)2469.

[19] J.Mares et al., Z.Phys.A **333**(1989)209.

[20] T.Motoba et al., Phys.Rev.C **38**(1988)1322.

[21] R.Bertini et al., Phys.Lett. **90B**(1980)375.

[22] R.Bertini et al., Phys.Lett. **136B**(1984)29.

[23] R.Bertini et al., Phys.Lett. **158B**(1985)19.

[24] H.Piekarz et al., Phys.Lett. **110B**(1982)428.

[25] L.Tang et al., Phys.Rev.C **39**(1988)846.

[26] R.S.Hayano et al., Phys.Lett. **231B**(1989)355.

[27] H.Bando et al., Int.J. of Mod.Phys. **5**(1990)4021.

[28] H.Bando et al., Z.Phys.A **330**(1988)203.

[29] H.J.Pirner, Phys.Lett. **85B**(1979)190.

[30] H.J.Pirner et al.,Phys.Lett. **114B**(1982)308.

[31] A.Bouyssy, Phys.Lett. **99B**(1981)305.

[32] R.Brockmann, Phys.Lett. **104B**(1981)256.

[33] T.Motoba, Nuevo Cimeto **102A**(1989)345.

[34] D.Marlow et al., Phys.Rev.C **25**(1982)2619.

[35] D.Marlow et al., Phys.Rev.C **30**(1984)1662.

[36] M.Cantin et al., Nucl.Instr. and Meth.**118**(1974)177.

[37] M.Bourdinaud et al., Nucl.Instr. and Meth.**136** (1976)99.

[38] G.Poelz et al., Nucl.Instr. and Meth.**195**(1982)491.

[39] M.Benot et al., Nucl.Instr. and Meth.**154**(1978)253.

[40] C.Arnault et al., Nucl.Instr. and Meth.**177**(1980)337.

[41] C.Arnault et al., Physica Scripta **23**(1981)710.

[42] P.J.Carlson et al., Physica Scripta **23**(1981)708.

[43] P.Carlson, Nucl.Instr. and Meth.**A248**(1986)110.

[44] H.Burkhardt et al., Nucl.Instr. and Meth.**184**(1981)319.

[45] Günter Poelz, Nucl.Instr. and Meth.**A248**(1986)118.

[46] P.J.Carlson et al., Nucl.Instr. and Meth.**166**(1979)425.

[47] J.P.De Brion et al., Nucl.Instr. and Meth.**179**(1981)61.

[48] S.Henning et al., Physica Scripta **23**(1981)703.

[49] H.Kawai et al., Nucl.Instr. and Meth.**228**(1985)314.

[50] E.W.Washburn et al. (ed.), "*International Critical Tables of Numerical Data, Physics, Chemistry and Technology*", McGraw-Hill Book Company, New York and London, (1929)261.

[51] J.Myrheim et al., Nucl.Instr. and Meth.**160**(1979)43.

[52] H.Grote, CERN/81-03(1981)136.

[53] K.Amako et al., Nucl.Instr. and Meth. **197**(1982)325.

[54] H.Bichsel et al.,Phys.Rev.A **11**(1975)1286.

[55] T.Motoba, private comunication.

[56] H.D.Maccabee et al., Phys.Lett.**30A**(1969)241.

[57] R.Talman, Nucl.Instr. and Meth.**159**(1979)189.

[58] Steven P.Ahlen, Rev.Mod.Phys.**52**(1980)121.